

# Discovery prospects for photophobic axion-like particles at a 100 TeV proton–proton collider

Zilong Ding<sup>a,b,1</sup>, Jiaojiao Feng<sup>a,1</sup>, Ying-nan Mao<sup>a,1</sup>, Kechen Wang<sup>a,1</sup> and Yiheng Xiong<sup>a,c,1</sup>

<sup>a</sup>*Department of Physics, School of Physics and Mechanics, Wuhan University of Technology, 430070 Wuhan, Hubei, China*

<sup>b</sup>*College of Physical Science and Technology, Central China Normal University, 430079 Wuhan, Hubei, China*

<sup>c</sup>*School of Physics, Beihang University, 102206, Beijing, China*

*E-mail:* [zilong.d@mails.ccnu.edu.cn](mailto:zilong.d@mails.ccnu.edu.cn), [jiaojiao.feng@whut.edu.cn](mailto:jiaojiao.feng@whut.edu.cn),  
[ynmao@whut.edu.cn](mailto:ynmao@whut.edu.cn), [kechen.wang@whut.edu.cn](mailto:kechen.wang@whut.edu.cn), [yihenght@buaa.edu.cn](mailto:yihenght@buaa.edu.cn)

**ABSTRACT:** We study heavy photophobic axion-like particles (ALPs) in the limit of an effectively vanishing diphoton coupling,  $g_{a\gamma\gamma} \simeq 0$ , for which diphoton production and decay are suppressed and collider phenomenology is driven by electroweak interactions ( $aWW$ ,  $aZ\gamma$ ,  $aZZ$ ). We perform detector-level searches at a future  $\sqrt{s} = 100$  TeV  $pp$  collider (SppC/FCC-hh), with an integrated luminosity of  $\mathcal{L} = 20 \text{ ab}^{-1}$ . We consider  $a \rightarrow Z\gamma$  and  $a \rightarrow W^+W^-$  decays. For  $pp \rightarrow jj a$  we include both  $s$ -channel electroweak exchange and vector boson fusion (VBF)-like topologies, while the tri- $W$  signature arises from associated production  $pp \rightarrow W^\pm a$  (via  $s$ -channel exchange) followed by  $a \rightarrow W^+W^-$ . We analyze three final states— $Z\gamma jj$  with  $Z \rightarrow \ell^+\ell^-$ , tri- $W$  ( $W^\pm W^\pm W^\mp$ ) with same-sign dimuons plus jets, and  $W^+W^- jj$  with opposite-sign, different-flavor dilepton ( $e^\pm\mu^\mp$ ) plus jets. A boosted-decision-tree (BDT) classifier built from kinematic observables provides the final signal–background separation. At  $\sqrt{s} = 100$  TeV and  $\mathcal{L} = 20 \text{ ab}^{-1}$ , we present discovery sensitivities to the ALP– $W$  coupling  $g_{aWW}$  over  $m_a \in [100, 7000]$  GeV. In parallel, we report model-independent discovery thresholds on  $\sigma \times \text{Br}$  for  $pp \rightarrow jj a$  with  $a \rightarrow Z\gamma$  and  $a \rightarrow W^+W^-$ , as well as for associated production  $pp \rightarrow W^\pm a$  with  $a \rightarrow W^+W^-$ . Taken together, the three channels deliver broad coverage and mutually reinforcing checks across decay modes and production regimes, strengthening robustness against channel-dependent systematics. The 100 TeV program extends the discovery reach well beyond 14 TeV projections within a general effective field theory (EFT) description that does not assume a specific ultraviolet completion.

<sup>1</sup>Corresponding author.

---

## Contents

<b>1</b>	<b>Introduction</b>	<b>2</b>
<b>2</b>	<b>Theory Models</b>	<b>3</b>
<b>3</b>	<b>Signal production</b>	<b>4</b>
<b>4</b>	<b>Backgrounds and data analysis</b>	<b>7</b>
4.1	$Z\gamma jj$ final state	7
4.1.1	Background processes	7
4.1.2	Preselection	7
4.1.3	Reconstruction of the ALP mass	8
4.1.4	Multivariate analysis	9
4.2	$W^\pm W^\pm W^\mp$ final state	11
4.2.1	Background processes	11
4.2.2	Preselection	11
4.2.3	Multivariate analysis	12
4.3	$W^+ W^- jj$ final state	14
4.3.1	Background processes	14
4.3.2	Preselection	15
4.3.3	Multivariate analysis	16
<b>5</b>	<b>Results</b>	<b>17</b>
5.1	Sensitivities on $g_{aWW}$	18
5.2	Sensitivities on production cross sections	20
<b>6</b>	<b>Conclusion</b>	<b>22</b>
<b>A</b>	<b>Details of the <math>Z\gamma jj</math> analyses</b>	<b>23</b>
A.1	Distributions of representative observables	23
A.2	Distributions of BDT responses	25
A.3	BDT selection efficiencies	25
<b>B</b>	<b>Details of the <math>W^\pm W^\pm W^\mp</math> analyses</b>	<b>26</b>
B.1	Distributions of representative observables	26
B.2	Distributions of BDT responses	29
B.3	Selection efficiencies	30

<b>C Details of the <math>W^+W^-jj</math> analyses</b>	<b>31</b>
C.1 Distributions of representative observables	31
C.2 Distributions of BDT responses	32
C.3 Selection efficiencies	33

---

## 1 Introduction

Axion-like particles (ALPs) are widely used effective descriptions of new pseudo-scalar states that couple to Standard-Model (SM) fields through higher-dimensional operators, and they provide a sharp target for collider searches in scenarios where the relevant degrees of freedom are electroweak gauge bosons. While the quantum chromodynamics (QCD) axion is tied to the Peccei–Quinn (PQ) solution of the strong-CP problem in QCD [1–12], collider-oriented ALP studies typically treat the mass and effective couplings as largely independent parameters [13–16], motivating broad experimental programs across astrophysical, laboratory, and high-energy frontiers [17–60].

Over a wide ALP mass range, existing laboratory, astrophysical, and collider searches place stringent bounds on the ALP–photon interaction, making the diphoton coupling  $g_{a\gamma\gamma}$  one of the most tightly constrained ALP portals [61–69]. This naturally motivates the photophobic limit, in which the effective  $a\gamma\gamma$  interaction is suppressed [70–72] and collider phenomenology is instead driven by electroweak couplings such as  $aWW$ ,  $aZ\gamma$ , and  $aZZ$ . Heavy photophobic ALPs are additionally of interest in light of the CDF II high-precision  $m_W$  result [68, 73], for which heavy ALPs with  $g_{a\gamma\gamma} \sim 0$  have been argued to improve electroweak precision fits when  $m_a \gtrsim 500$  GeV [74].

At the LHC, constraints on heavy photophobic ALPs have been widely obtained by reinterpreting analyses optimized for SM targets—including triboson searches at  $\sqrt{s} = 8$  TeV [70], vector boson scattering (VBS)-motivated selections interpreted as nonresonant ALP exchange [75], and Run-2 analyses targeting  $W^\pm W^\pm W^\mp$  and  $Z\gamma$  final states [76]; see Ref. [77] for a recent overview. Because the signal hypotheses and control strategies were not designed for on-shell ALP production, acceptance and kinematic mismatches can make such recast constraints conservative and non-uniform across parameter space.

To address this, our group has developed a coordinated set of detector-level HL-LHC projections for photophobic ALPs at  $\sqrt{s} = 14$  TeV and  $\mathcal{L} = 3 \text{ ab}^{-1}$  [77–79], using mass-dependent multivariate discrimination optimized for each hypothesis. These studies cover (i)  $pp \rightarrow jj a(\rightarrow Z\gamma)$  with  $Z \rightarrow \ell^+\ell^-$  ( $\ell = e, \mu$ ), including both  $s$ -channel and vector boson fusion (VBF)-like production, for  $m_a \simeq 100\text{--}4000$  GeV [77]; (ii) a tri- $W$  strategy  $pp \rightarrow W^\pm X(\rightarrow W^+W^-)$  in a same-sign dimuon plus hadronic- $W$  final state, for  $m_a \simeq 170\text{--}3000$  GeV [78]; and (iii)  $pp \rightarrow jj a(\rightarrow W^+W^-)$  in the  $e^\pm\mu^\mp + \cancel{E}_T$  channel, for  $m_a \simeq 170\text{--}4000$  GeV [79].

In this work, we turn to a future proton–proton ( $pp$ ) collider with  $\sqrt{s} \sim \mathcal{O}(100)$  TeV, such as the Super proton–proton Collider (SppC) or the Future Circular Collider in hadron–hadron mode (FCC-hh) [80–85]. We study heavy photophobic ALPs in the limit  $g_{a\gamma\gamma} \simeq 0$ , focusing on ALPs coupled to electroweak field strengths. We perform dedicated detector-level searches in three complementary channels: (I)  $pp \rightarrow jj a (\rightarrow Z\gamma)$  with  $Z \rightarrow \ell^+\ell^-$  ( $\ell = e, \mu$ ); (II)  $pp \rightarrow W^\pm a (\rightarrow W^\pm W^\mp)$  with a same-sign dimuon signature plus a hadronic decayed  $W$  boson; and (III)  $pp \rightarrow jj a (\rightarrow W^\pm W^\mp)$  with opposite-sign, different-flavor dilepton  $e^\pm \mu^\mp$ . Our analysis incorporates the relevant production topologies— $s$ -channel exchange and, where applicable, VBF-like configurations—models signal and backgrounds consistently with detector-level simulations, and employs a boosted decision tree (BDT)-based multivariate analysis (MVA) optimized for each mass hypothesis. We present projected sensitivities over  $m_a = 100$ –7000 GeV, reporting both discovery reaches on  $g_{aWW}$  and model-independent discovery thresholds on the fiducial quantity given by the signal production cross section times branching ratio,  $\sigma \times \text{Br}$ . The three final states probe the same photophobic setup from different experimental angles, which strengthens the interpretation by reducing the reliance on any single background model and by helping pinpoint whether any emerging excess prefers  $Z\gamma$  or  $WW$  decays and which production regime dominates.

This paper is organized as follows. Sec. 2 lays out the theoretical framework. Sec. 3 introduces the signal topologies and the event generation setup. Sec. 4 presents the analysis strategy and background modeling for each final state, including preselection, ALP-mass reconstruction where applicable, and the MVA approach. Sec. 5 shows the main results, followed by the conclusion in Sec. 6. Additional material is provided in the appendices.

## 2 Theory Models

We adopt an effective-field-theory description of a pseudoscalar axion-like particle (ALP) whose leading interactions are restricted to the electroweak gauge-field strengths. Keeping the dimension-five operators prior to electroweak symmetry breaking (EWSB), the relevant terms can be written as [86]

$$\mathcal{L}_{\text{ALP}} \supset \frac{1}{2} \partial_\mu a \partial^\mu a - \frac{1}{2} m_a^2 a^2 - \frac{c_{\widetilde{W}}}{f_a} a W_{\mu\nu}^b \widetilde{W}^{b,\mu\nu} - \frac{c_{\widetilde{B}}}{f_a} a B_{\mu\nu} \widetilde{B}^{\mu\nu}, \quad (2.1)$$

where  $a$  and  $m_a$  denote the ALP field and its mass, and  $f_a$  is the associated decay constant. Here  $W_{\mu\nu}^b$  ( $b = 1, 2, 3$ ) and  $B_{\mu\nu}$  are the SU(2)<sub>L</sub> and U(1)<sub>Y</sub> field strengths, and the dual tensor is defined as  $\widetilde{X}^{\mu\nu} \equiv \frac{1}{2} \epsilon^{\mu\nu\alpha\beta} X_{\alpha\beta}$  with  $X = W^b, B$ . In practice, physical observables depend on the ratios  $c_{\widetilde{W}}/f_a$  and  $c_{\widetilde{B}}/f_a$ , and we treat  $(m_a, c_{\widetilde{W}}/f_a, c_{\widetilde{B}}/f_a)$  as independent inputs at this stage.

After EWSB, rotating to the mass eigenstates  $A$ ,  $Z$ , and  $W^\pm$ , the interactions can be organized as

$$\mathcal{L}_{\text{int}} \supset -\frac{1}{4} g_{a\gamma\gamma} a F_{\mu\nu} \widetilde{F}^{\mu\nu} - \frac{1}{2} g_{aZ\gamma} a Z_{\mu\nu} \widetilde{F}^{\mu\nu} - \frac{1}{4} g_{aZZ} a Z_{\mu\nu} \widetilde{Z}^{\mu\nu} - \frac{1}{2} g_{aWW} a W_{\mu\nu}^+ \widetilde{W}^{-\mu\nu}, \quad (2.2)$$

with the tree-level relations

$$g_{a\gamma\gamma} = \frac{4}{f_a} (s_\theta^2 c_{\widetilde{W}} + c_\theta^2 c_{\widetilde{B}}), \quad (2.3)$$

$$g_{aZZ} = \frac{4}{f_a} (c_\theta^2 c_{\widetilde{W}} + s_\theta^2 c_{\widetilde{B}}), \quad (2.4)$$

$$g_{aZ\gamma} = \frac{2}{f_a} s_{2\theta} (c_{\widetilde{W}} - c_{\widetilde{B}}), \quad (2.5)$$

$$g_{aWW} = \frac{4}{f_a} c_{\widetilde{W}}, \quad (2.6)$$

where  $\theta$  is the weak mixing angle and we use the shorthand  $s_\theta \equiv \sin \theta$ ,  $c_\theta \equiv \cos \theta$ , and  $s_{2\theta} \equiv \sin 2\theta$  for simplicity.

Motivated by the strict experimental bounds on the diphoton channel, we work in the *photophobic* limit,

$$g_{a\gamma\gamma} = 0 \iff s_\theta^2 c_{\widetilde{W}} + c_\theta^2 c_{\widetilde{B}} = 0 \iff c_{\widetilde{B}} = -t_\theta^2 c_{\widetilde{W}}, \quad (2.7)$$

where  $t_\theta \equiv \tan \theta$ . With this condition imposed at tree level, the remaining electroweak couplings are correlated as

$$g_{aZ\gamma} = t_\theta g_{aWW}, \quad g_{aZZ} = (1 - t_\theta^2) g_{aWW}. \quad (2.8)$$

Throughout our phenomenological analysis we scan  $(m_a, g_{aWW})$  and fix  $g_{aZ\gamma}$  and  $g_{aZZ}$  using the above relations.

Beyond tree level, radiative corrections and renormalization-group running effects can regenerate a small effective  $g_{a\gamma\gamma}$  even when the photophobic condition is imposed. For the collider study presented here, this correction is numerically negligible [20, 70, 77, 87, 88], and we neglect it.

### 3 Signal production

Although a photophobic ALP does not couple to diphoton at tree level, it still couples to the electroweak diboson states ( $aWW$ ,  $aZZ$ , and  $aZ\gamma$ ). Heavy ALPs can therefore be produced at colliders via these effective vertices. Fig. 1 illustrates the signal topologies considered in this study, namely ALP production in association with two jets at the SppC/FCC-hh, either via an  $s$ -channel electroweak gauge boson or via vector-boson fusion (VBF). Panel (I) of Fig. 1 corresponds to  $pp \rightarrow jj a(\rightarrow Z\gamma)$ , where the  $Z$  boson decays dileptonically,  $Z \rightarrow \ell^+ \ell^-$  with  $\ell = e, \mu$ . Panel (II) shows  $pp \rightarrow W^\pm a(\rightarrow W^\pm W^\mp)$ , where the same-sign  $W$  bosons decay leptonically into muons and neutrinos,  $W^\pm \rightarrow \mu^\pm \nu_\mu / \bar{\nu}_\mu$ , while the remaining  $W$  boson decays hadronically,  $W^\mp \rightarrow jj$ . Panel (III) corresponds to  $pp \rightarrow jj a(\rightarrow W^\pm W^\mp)$ , where the two  $W$  bosons decay leptonically into different-flavor dilepton,  $e^\pm \mu^\mp$ , each accompanied by the corresponding neutrino. The diagrams in panel (II) and the upper diagrams of (I) and (III) represent associated production via an  $s$ -channel gauge boson, while the lower diagrams of (I) and (III) represent VBF production with two forward jets.

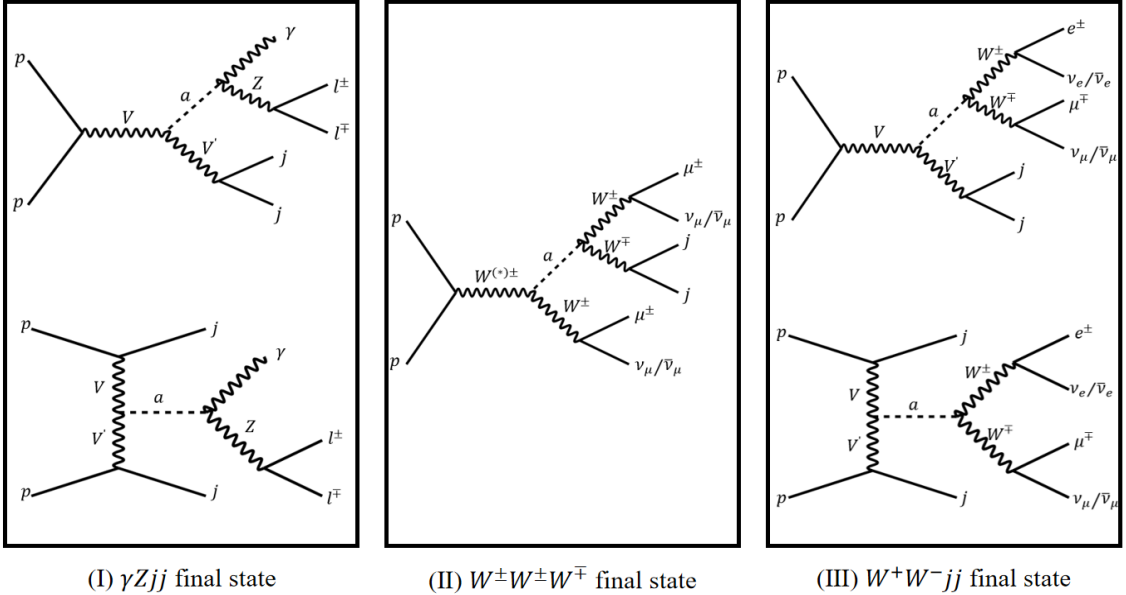


**Figure 1:** Signal production and decay topologies for the photophobic ALP considered in this work. (I)  $pp \rightarrow jj a (\rightarrow Z\gamma)$  with  $Z \rightarrow \ell^+\ell^-$  ( $\ell = e, \mu$ ); (II)  $pp \rightarrow W^\pm a (\rightarrow W^\pm W^\pm W^\mp)$ , where the same-sign  $W$  bosons decay leptonically into muons and neutrinos,  $W^\pm \rightarrow \mu^\pm \nu_\mu/\bar{\nu}_\mu$ , while the remaining  $W$  boson decays hadronically,  $W^\mp \rightarrow jj$ ; (III)  $pp \rightarrow jj a (\rightarrow W^+ W^-)$ , where the two  $W$  bosons decay leptonically into different-flavor dilepton,  $e^\pm \mu^\mp$ .

To generate the signal events, we implement the ALP model based on the linear Lagrangian [89] in the Universal FeynRules Output (UFO) format [90] and import it into the MadGraph5\_aMC@NLO framework (version 2.6.7) [91] to simulate  $pp$  collisions, using the default “nn23lo1” parton distribution function (PDF) set [92]. Parton showering and hadronization are simulated with PYTHIA 8.3 [93], which also handles the decays of unstable SM particles. Detector effects are modeled with Delphes 3.4.2 [94] using the CMS configuration card. Jets are reconstructed with FastJet [95] employing the anti- $k_t$  algorithm [96] with radius parameter  $R = 0.4$ .

For signal (I), we generate  $pp \rightarrow jj a (\rightarrow Z\gamma)$  events with MadGraph, and allow  $Z \rightarrow \ell^+\ell^-$  with  $\ell = e, \mu, \tau$  at the generator level, while in the analysis we restrict to final states with  $\ell = e, \mu$ . We generate samples at representative ALP masses  $m_a \in \{100, 165, 400, 700, 1000, 1500, 2000, 4000, 5000, 7000\}$  GeV. For each  $m_a$ , the coupling is fixed to the benchmark value  $g_{aWW} = 1 \text{ TeV}^{-1}$ , and at least  $10^6$  events are generated.

For signal (II), we generate  $pp \rightarrow W^\pm a (\rightarrow W^\pm W^\pm W^\mp)$  events with MadGraph. We generate samples at representative ALP masses  $m_a \in \{170, 200, 300, 400, 600, 900, 1400, 1800, 2200, 3000, 5000, 10000, 20000\}$  GeV. For each mass point, the coupling is fixed to  $g_{aWW} = 1 \text{ TeV}^{-1}$ , and at least  $10^6$  events are generated.

For signal (III), the hard-scattering process  $pp \rightarrow jj a$  is generated with MadGraph, while the subsequent decays  $a \rightarrow W^+ W^-$  and  $W^\pm \rightarrow \ell^\pm \nu$ ,  $W^\pm \rightarrow \ell^\pm \bar{\nu}$  ( $\ell = e, \mu$ ), yielding

$a \rightarrow W^+(\rightarrow \ell^+ \nu) W^-(\rightarrow \ell^- \bar{\nu}) jj$ , are simulated with PYTHIA 8.3. We generate signal samples at representative ALP masses  $m_a \in \{170, 185, 200, 225, 250, 350, 750, 1500, 2500, 4000, 5500, 7000\}$  GeV. At the HL-LHC, we generate 1.0 and 0.305 million events for the benchmark points  $m_a = 200$  and 225 GeV, respectively; 0.3 million events for each point with  $m_a = 170, 185$  and 250 GeV; and 0.275 million events for each point with  $m_a = 350, 750, 1500, 2500, 4000, 5500$  and 7000 GeV.

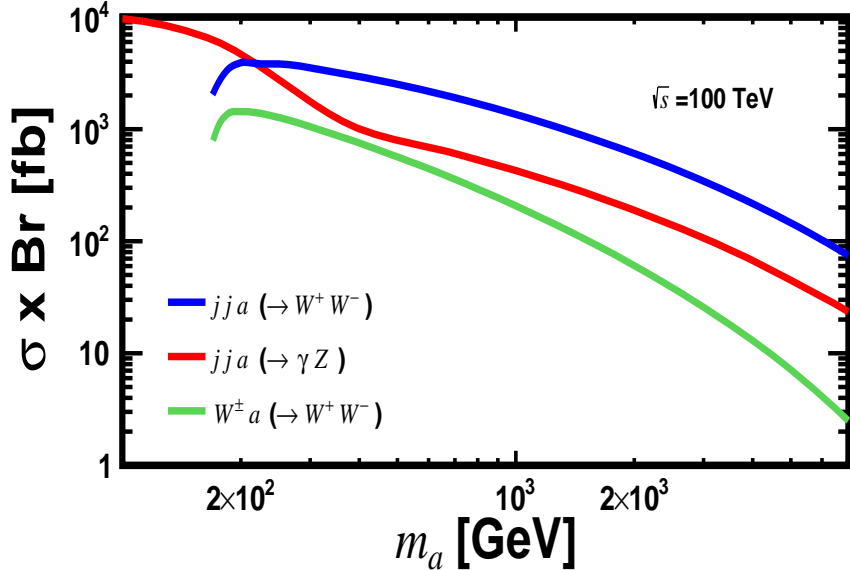


**Figure 2:** Assuming benchmark couplings  $g_{a\gamma\gamma} = 0$  and  $g_{aWW} = 1 \text{ TeV}^{-1}$  at the SppC/FCC-hh with  $\sqrt{s} = 100$  TeV, the production cross section times branching ratio,  $\sigma(pp \rightarrow jj a) \times \text{Br}(a \rightarrow Z\gamma)$ , is shown as a function of the ALP mass  $m_a$  in the range 100–7000 GeV, while  $\sigma(pp \rightarrow W^\pm a) \times \text{Br}(a \rightarrow W^\pm W^-)$  and  $\sigma(pp \rightarrow jj a) \times \text{Br}(a \rightarrow W^\pm W^-)$  are shown as functions of  $m_a$  in the range 170–7000 GeV. The red, green, and blue curves correspond to  $jj a(\rightarrow Z\gamma)$ ,  $W^\pm a(\rightarrow W^\pm W^-)$ , and  $jj a(\rightarrow W^\pm W^-)$ , respectively.

In Fig. 2, we present the rates  $\sigma \times \text{Br}$  for the three signal processes as functions of  $m_a$  at  $\sqrt{s} = 100$  TeV, for  $g_{a\gamma\gamma} = 0$  and  $g_{aWW} = 1 \text{ TeV}^{-1}$ . All curves fall with increasing  $m_a$ , reflecting the rapidly decreasing parton luminosities at large momentum fractions. For  $jj a(\rightarrow Z\gamma)$  (red), a pronounced suppression around  $m_a \sim 200$  GeV is mainly due to the opening of competing two-body diboson channels, which quickly depletes  $\text{Br}(a \rightarrow Z\gamma)$  over  $m_a \simeq 160$ –250 GeV [77]. For the  $W^\pm W^-$  modes (blue and green),  $\text{Br}(a \rightarrow W^\pm W^-)$  turns on rapidly above the threshold  $m_a \simeq 2m_W$  (e.g.  $\sim 49\%$  at  $m_a = 185$  GeV [74, 77]) and then varies only mildly at higher masses; together with the falling production cross sections, this yields a broad maximum in  $\sigma \times \text{Br}$  just above threshold, around  $m_a \sim 190$ –200 GeV. For the associated-production channel  $pp \rightarrow W^\pm a(\rightarrow W^\pm W^-)$  (green), the point shown at  $m_a = 7000$  GeV is obtained by a smooth fit to the simulated mass points (including samples generated at higher masses).

## 4 Backgrounds and data analysis

### 4.1 $Z\gamma jj$ final state

#### 4.1.1 Background processes

Since the final state contains one photon, an opposite-sign same-flavor lepton pair, and two jets, we consider six relevant SM background processes:  $ZW\gamma$ ,  $Z(\rightarrow \ell^+\ell^-)\gamma jj$ ,  $ZZ\gamma$ ,  $W^+W^-\gamma$ ,  $W(\rightarrow \ell\nu)\gamma jj$ , and  $t\bar{t}\gamma$ , where  $\ell = e, \mu, \tau$  denotes a charged lepton and  $\nu$  denotes an (anti)neutrino. We label them as “B1–B6” throughout. When a  $Z$  boson decays to  $\ell^+\ell^-$  and the accompanying heavy  $W/Z$  boson decays hadronically, B1–B3 yield the same visible final state as the signal and are thus irreducible. B4–B5 can contribute via misidentified leptons in the reconstruction. If both  $W$  bosons in the final state decay leptonically, B6 also contributes.

Background events are generated with the same tool chain as the signal (MadGraph + PYTHIA + Delphes [91–94]). Event yields for both signal and backgrounds are normalized using the production cross sections reported by MadGraph5\_aMC@NLO. To reduce statistical uncertainties, we produce as many background events as allowed by our computing resources. In total we generate 10.0 million  $ZW\gamma$ , 22.0 million  $Z(\rightarrow \ell^+\ell^-)\gamma jj$ , 10.0 million  $ZZ\gamma$ , 10.0 million  $W^+W^-\gamma$ ,  $1.0 \times 10^9$   $W(\rightarrow \ell\nu)\gamma jj$ , and 18.0 million  $t\bar{t}\gamma$  events. Due to their large production cross sections, B2 and B5 dominate the total background. To improve generating efficiency for B2 and B5, we force the  $Z/W$  bosons to decay leptonically at the generator level, i.e.  $Z \rightarrow \ell^+\ell^-$  and  $W \rightarrow \ell\nu$  with  $\ell = e, \mu, \tau$ .

#### 4.1.2 Preselection

Final-state objects (photons, leptons, and jets) are ordered by transverse momentum and labeled  $O_i$  with  $O = \gamma, \ell, j$  and  $i = 1, 2, \dots$ . We apply the following preselection criteria as the first selection step to target the desired final state and suppress backgrounds:

- (i) At least one photon,  $N(\gamma) \geq 1$ , with  $p_T(\gamma_1) > 20$  GeV.
- (ii) Exactly two same-flavor, opposite-sign leptons ( $\ell = e, \mu$ ), i.e.  $N(\ell) = 2$  and an  $\ell^+\ell^-$  pair, with  $p_T(\ell_{1,2}) > 20$  GeV.
- (iii) At least two jets,  $N(j) \geq 2$ , with  $p_T(j_{1,2}) > 50$  GeV.
- (iv) No  $b$ -tagged or  $\tau$ -tagged jets:  $N(j_b) = 0$  and  $N(j_\tau) = 0$ .

The expected number of events,  $N_{\text{exp}}$ , is computed as

$$N_{\text{exp}} = \sigma_{\text{pro}} \times \mathcal{L} \times \epsilon_{\text{sel}}, \quad (4.1)$$

where  $\sigma_{\text{pro}}$  is the production cross section of the process,  $\mathcal{L}$  is the integrated luminosity, and  $\epsilon_{\text{sel}}$  is the selection efficiency obtained from our analysis. Table 1 shows event yields for the signal with benchmark  $m_a = 700$  GeV and for each background process after applying

SppC/FCC-hh		initial	(i)	(ii)	(iii)	(iv)
signal	$jj a(\rightarrow Z\gamma(\rightarrow \ell^+\ell^-))$	$1.2 \times 10^6$	$1.1 \times 10^6$	$4.3 \times 10^5$	$3.7 \times 10^5$	$2.8 \times 10^5$
	total background	$7.6 \times 10^{10}$	$1.7 \times 10^{10}$	$2.1 \times 10^8$	$7.5 \times 10^7$	$4.8 \times 10^7$
B1	$ZW\gamma$	$5.2 \times 10^7$	$2.1 \times 10^7$	$4.8 \times 10^5$	$3.2 \times 10^5$	$3.1 \times 10^4$
B2	$Z(\rightarrow \ell^+\ell^-)\gamma jj$	$6.6 \times 10^9$	$1.0 \times 10^9$	$1.7 \times 10^8$	$5.1 \times 10^7$	$4.5 \times 10^7$
B3	$ZZ\gamma$	$2.0 \times 10^7$	$6.1 \times 10^6$	$3.6 \times 10^5$	$7.7 \times 10^4$	$5.2 \times 10^4$
B4	$W^+W^-\gamma$	$1.4 \times 10^8$	$4.1 \times 10^7$	$1.1 \times 10^6$	$6.8 \times 10^4$	$5.4 \times 10^4$
B5	$W(\rightarrow \ell\nu)\gamma jj$	$6.6 \times 10^{10}$	$1.5 \times 10^{10}$	$1.8 \times 10^6$	$1.0 \times 10^6$	$5.9 \times 10^5$
B6	$t\bar{t}\gamma$	$3.4 \times 10^9$	$1.4 \times 10^9$	$3.2 \times 10^7$	$2.3 \times 10^7$	$1.9 \times 10^6$

**Table 1:** Event yields for the signal with benchmark  $m_a = 700$  GeV and for each background process after applying preselection criteria (i)–(iv) sequentially. Numbers correspond to the SppC/FCC-hh with  $\sqrt{s} = 100$  TeV and  $\mathcal{L} = 20$  ab $^{-1}$ .

$m_a$ [GeV]	100	165	400	700	1000	1500
	$4.34 \times 10^{-2}$	$1.27 \times 10^{-1}$	$20.2 \times 10^{-1}$	$2.29 \times 10^{-1}$	$2.43 \times 10^{-1}$	$2.56 \times 10^{-1}$
$m_a$ [GeV]	2000	4000	5000	7000		
	$2.63 \times 10^{-1}$	$2.76 \times 10^{-1}$	$2.79 \times 10^{-1}$	$2.83 \times 10^{-1}$		
background	B1	B2	B3	B4	B5	B6
	$ZW\gamma$	$Z(\rightarrow \ell^+\ell^-)\gamma jj$	$ZZ\gamma$	$W^+W^-\gamma$	$W(\rightarrow \ell\nu)\gamma jj$	$t\bar{t}\gamma$
	$5.96 \times 10^{-4}$	$6.88 \times 10^{-3}$	$2.60 \times 10^{-3}$	$3.86 \times 10^{-4}$	$8.94 \times 10^{-6}$	$5.59 \times 10^{-4}$

**Table 2:** Preselection efficiencies for the signal with representative ALP masses and for the background processes at the SppC/FCC-hh with  $\sqrt{s} = 100$  TeV.

preselection criteria (i)–(iv) sequentially. Numbers correspond to the SppC/FCC-hh with  $\sqrt{s} = 100$  TeV and  $\mathcal{L} = 20$  ab $^{-1}$ .

Table 2 shows the selection efficiencies after applying criteria (i)–(iv) for representative  $m_a$  values and for all background processes at  $\sqrt{s} = 100$  TeV. One observes that B5 is strongly rejected, with a preselection efficiency of  $8.94 \times 10^{-6}$ . Efficiencies for the other backgrounds are typically  $\sim 10^{-3}$ – $10^{-4}$ . It is worth noting that, for the signal, the preselection efficiency at  $m_a = 100$  GeV is  $4.34 \times 10^{-2}$ , smaller than for other masses. This is because  $m_a$  is close to the  $Z$ -boson mass, yielding softer photons.

#### 4.1.3 Reconstruction of the ALP mass

Since the signal contains  $a \rightarrow Z\gamma$  with  $Z \rightarrow \ell^+\ell^-$ , we reconstruct  $m_a$  from the invariant mass of the system formed by the two leading leptons and the leading photon, denoted as  $m(\ell_1 + \ell_2 + \gamma_1)$ . Fig. 3 shows the corresponding  $m(\ell_1 + \ell_2 + \gamma_1)$  distributions for the total background (dotted) and for signal benchmarks with various  $m_a$ , after preselection at  $\sqrt{s} = 100$  TeV. One observes that the signal peaks sharply near the input value of  $m_a$  throughout the range 100–7000 GeV, whereas the total background exhibits a broad

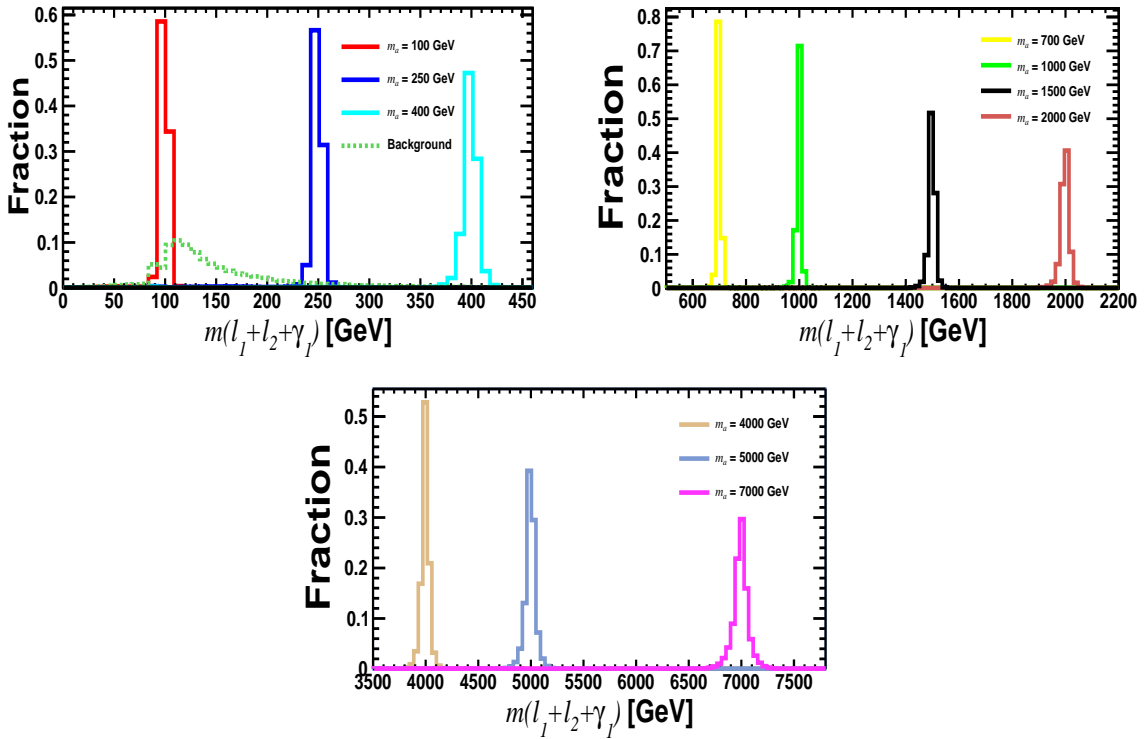


**Figure 3:** Distributions of the invariant mass of the system formed by the two leading leptons and the leading photon,  $m(\ell_1 + \ell_2 + \gamma_1)$ , for the total background (dotted) and for signal benchmarks with various  $m_a$ , after preselection at  $\sqrt{s} = 100$  TeV.

structure around  $\sim 130$  GeV. Thus, the invariant mass  $m(\ell_1 + \ell_2 + \gamma_1)$  provides a reliable estimator of the ALP mass and a powerful discriminator for  $m_a \gtrsim 200$  GeV.

#### 4.1.4 Multivariate analysis

After preselection, to further suppress backgrounds, we train a BDT using TMVA with its default settings [97]. The input observables are organized as follows:

- (A) Kinematics of the leading objects:  $E(O)$ ,  $p_T(O)$ ,  $\eta(O)$ , and  $\phi(O)$  for  $O = \gamma_1, \ell_1, \ell_2, j_1, j_2$ .
- (B) Missing-momentum observables:  $\not{E}_T$  and its azimuthal angle  $\phi(\not{E}_T)$ .
- (C) Angular separations  $\Delta R \equiv \sqrt{(\Delta\eta)^2 + (\Delta\phi)^2}$ :  $\Delta R(j_1, j_2)$  and  $\Delta R(\gamma_1, \ell_1 + \ell_2)$ , where “ $\ell_1 + \ell_2$ ” denotes the dilepton system.
- (D) Invariant masses of combined systems:  $m(j_1 + j_2)$  and  $m(\ell_1 + \ell_2 + \gamma_1)$ .
- (E) Over all dijet pairs, the minimal angular separation and the corresponding invariant mass:  $\Delta R(j, j')_{\min}$  and  $m(j + j')_{\min \Delta R}$ .
- (F) Over all dijet pairs, the maximal pseudorapidity separation and the corresponding invariant mass:  $\Delta\eta(j, j')_{\max}$  and  $m(j + j')_{\max \Delta\eta}$ .

Appendix A.1 presents distributions of representative observables for the signal with benchmark  $m_a = 700$  GeV and for the six background processes at the SppC/FCC-hh with  $\sqrt{s} = 100$  TeV, after the preselection criteria are applied. As expected,  $m(\ell\ell\gamma)$  is a key discriminator across all masses. Given that the VBF contribution becomes increasingly important at larger  $m_a$ , we include variables that capture its topology (e.g., the dijet pair with maximal  $|\Delta\eta|$  and its invariant mass). For the  $s$ -channel topology, we instead use the dijet pair with minimal  $\Delta R$  and its invariant mass.

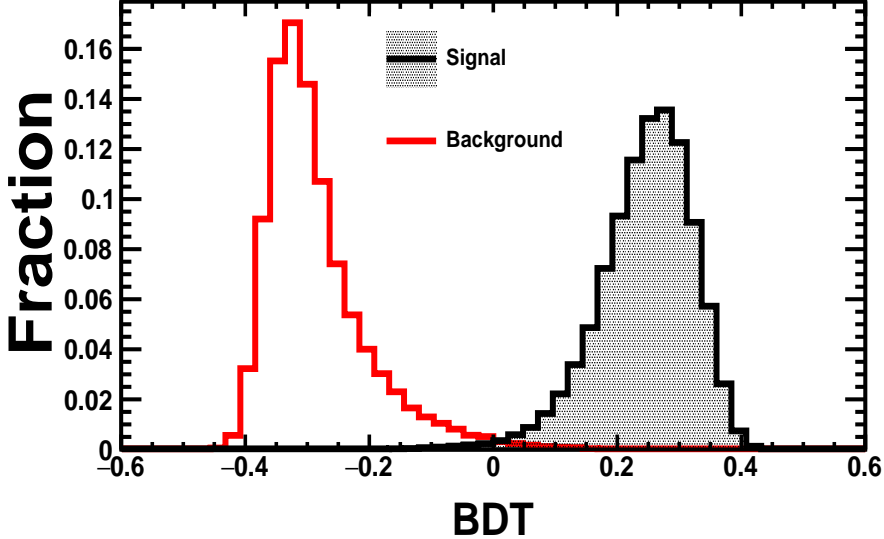


**Figure 4:** Distributions of BDT responses for the benchmark signal with  $m_a = 700$  GeV (black, shaded) and the total SM background (red) at the SppC/FCC-hh with  $\sqrt{s} = 100$  TeV.

Fig. 4 shows the BDT response distributions for the benchmark signal with  $m_a = 700$  GeV (black, shaded) and for the total SM background (red). Appendix A.2 presents the BDT response distributions for the signal and for the six background processes at the SppC/FCC-hh with  $\sqrt{s} = 100$  TeV, for different  $m_a$  values. As  $m_a$  increases, the BDT separation between signal and background improves, and for  $m_a \gtrsim 700$  GeV the overlap becomes small.

The BDT threshold is optimized independently at each  $m_a$  to maximize the statistical significance [98],

$$\sigma_{\text{stat}} = \sqrt{2 \left[ (N_s + N_b) \ln \left( 1 + \frac{N_s}{N_b} \right) - N_s \right]}, \quad (4.2)$$

where  $N_s$  ( $N_b$ ) denotes the number of signal (background) events after preselection and the BDT requirement [98–100]. The selection efficiencies of the optimized BDT requirement for both signal and background processes at the SppC/FCC-hh with  $\sqrt{s} = 100$  TeV, for different  $m_a$  values, are summarized in Appendix A.3.

## 4.2 $W^\pm W^\pm W^\mp$ final state

### 4.2.1 Background processes

The signal process is  $pp \rightarrow W^\pm a (\rightarrow W^\pm W^\mp)$ , where the same-sign  $W$  bosons decay leptonically into muons and neutrinos,  $W^\pm \rightarrow \mu^\pm \nu_\mu$  (including the charge-conjugate mode), while the remaining  $W$  boson decays hadronically,  $W^\mp \rightarrow jj$ ; cf. panel (II) of Fig. 1. The resulting final state contains two same-sign muons, a dijet system, and moderate missing transverse energy. The relevant SM processes that can mimic this signature are:

- (a) single-boson production with two jets:  $W^\pm jj$  and  $Zjj$ ;
- (b) diboson production with two jets:  $W^\pm W^\pm jj$ ,  $W^+ W^- jj$ ,  $W^\pm Zjj$ , and  $ZZjj$ ;
- (c) triboson production:  $W^\pm W^\pm W^\mp$ ;
- (d) top-quark pair production:  $t\bar{t}$ .

After the  $W$ -boson decays, the processes  $W^\pm W^\pm jj$  and  $W^\pm W^\pm W^\mp$  yield the same visible final state as the signal and therefore constitute irreducible backgrounds, despite their relatively small production cross sections. The  $W^\pm jj$  process, with a much larger production cross section, contributes via misidentified leptons. Charge mismeasurement of final-state leptons can also give rise to backgrounds from  $Zjj$ ,  $W^+ W^- jj$ , and  $t\bar{t}$ . Furthermore, the  $W^\pm Zjj$  process becomes relevant when one lepton is not reconstructed (a lost lepton), and  $ZZjj$  can contribute through either lost leptons or charge mismeasurement.

### 4.2.2 Preselection

We apply the following preselection criteria before performing the multivariate analysis. Final-state muons and jets are ordered by transverse momentum and labeled as  $O_i$  ( $i = 1, 2, \dots$ ) with  $O = \mu, j$ :

- (i) Exactly two muons, i.e.  $N(\mu) = 2$ .
- (ii) Both muons must satisfy  $p_T(\mu) > 10$  GeV.
- (iii) The two muons must have the same electric charge, i.e.  $\mu^\pm \mu^\pm$ .
- (iv) Each jet must satisfy  $p_T(j) > 30$  GeV.
- (v) At least two jets,  $N(j) \geq 2$ , and no  $b$ -tagged jets, i.e.  $N(j_b) = 0$ .

To illustrate the impact of each preselection criterion, Table 3 shows the expected number of events for the signal with benchmark  $m_a = 900$  GeV and for each background process after sequentially applying criteria (i)–(v) at the SppC/FCC-hh with  $\sqrt{s} = 100$  TeV and integrated luminosity  $\mathcal{L} = 20 \text{ ab}^{-1}$ . Because of its large production cross section and relatively high selection efficiency, the  $W^\pm jj$  background dominates and accounts for about 95% of the total background after preselection. As shown in Table 3, after applying all preselection criteria, the number of background events for most processes is reduced by at least a factor of  $10^4$ , although the total background still exceeds the expected signal yield.

	initial	(i)–(ii)	(iii)	(iv)–(v)
$W^\pm a(\rightarrow W^\pm W^\mp)$	$4.90 \times 10^6$	$1.31 \times 10^5$	$4.35 \times 10^4$	$2.48 \times 10^4$
$W^\pm(\rightarrow \mu^\pm \nu_\mu) jj$	$1.75 \times 10^{12}$	$2.82 \times 10^8$	$1.23 \times 10^8$	$5.20 \times 10^7$
$Z(\rightarrow \mu^+ \mu^-) jj$	$1.73 \times 10^{11}$	$1.12 \times 10^{11}$	$3.86 \times 10^6$	$1.48 \times 10^6$
$W^\pm W^\pm jj$	$1.21 \times 10^8$	$1.12 \times 10^6$	$1.11 \times 10^6$	$7.50 \times 10^5$
$W^\pm(\rightarrow \mu^\pm \nu_\mu) W^\mp jj$	$6.39 \times 10^9$	$5.04 \times 10^8$	$5.91 \times 10^5$	$3.45 \times 10^5$
$W^\pm Z jj$	$1.79 \times 10^{10}$	$3.32 \times 10^8$	$9.23 \times 10^6$	$5.62 \times 10^6$
$ZZ jj$	$3.38 \times 10^9$	$1.38 \times 10^8$	$2.04 \times 10^5$	$1.24 \times 10^5$
$W^\pm W^\pm W^\mp$	$3.16 \times 10^7$	$7.20 \times 10^5$	$2.36 \times 10^5$	$1.22 \times 10^5$
$t\bar{t}$	$4.94 \times 10^{11}$	$4.38 \times 10^9$	$5.05 \times 10^7$	$1.27 \times 10^7$

**Table 3:** Expected number of events for the signal with benchmark mass  $m_a = 900$  GeV and coupling  $g_{aWW} = 1$  TeV $^{-1}$ , and for the background processes, after applying preselection criteria (i)–(v) sequentially at the SppC/FCC-hh with  $\sqrt{s} = 100$  TeV and  $\mathcal{L} = 20$  ab $^{-1}$ .

#### 4.2.3 Multivariate analysis

After the preselection, we employ the TMVA package [97] to perform a MVA using a BDT with default settings. Events that pass the preselection are evaluated using the following kinematic observables:

- (A) Missing transverse energy and its azimuthal angle:  $\cancel{E}_T$  and  $\phi(\cancel{E}_T)$ .
- (B) The momentum components ( $p_x, p_y, p_z$ ) and energy ( $E$ ) of the two leading jets and two leading muons:  
 $p_x(j_1), p_y(j_1), p_z(j_1), E(j_1); p_x(j_2), p_y(j_2), p_z(j_2), E(j_2);$   
 $p_x(\mu_1), p_y(\mu_1), p_z(\mu_1), E(\mu_1); p_x(\mu_2), p_y(\mu_2), p_z(\mu_2), E(\mu_2).$
- (C) The number of charged tracks ( $N_{\text{track}}$ ) and the hadronic-to-electromagnetic energy ratio ( $R_E$ ) for the two leading jets:  
 $N_{\text{track}}(j_1), N_{\text{track}}(j_2); R_E(j_1), R_E(j_2)$  (typically  $R_E > 1$  for jets).
- (D) Angular separation and invariant mass of the two leading jets, and the jet multiplicity:  
 $\Delta R(j_1, j_2), m(j_1 + j_2), N(j).$
- (E) Muon-isolation observables:
  - (i) the scalar  $p_T$  sum of all other objects within a cone  $R = 0.4$  around the muon, excluding the muon itself:  $p_T^{\text{iso}}(\mu_1), p_T^{\text{iso}}(\mu_2)$ , and their maximum,  $p_{T,\text{max}}^{\text{iso}}(\mu)$ ;
  - (ii) the ratio of the transverse energy in a  $3 \times 3$  grid surrounding the muon to the muon transverse momentum (the “etrat” variable in Ref. [101]), which takes values between 0 and 0.99:  $R_{\text{grid}}(\mu_1), R_{\text{grid}}(\mu_2)$ ;
  - (iii) the minimal separation between each muon and any jet,  $\Delta R_{\text{min}}(\mu, j)$ . Well-isolated muons have small  $p_T^{\text{iso}}$  and  $R_{\text{grid}}$  but large  $\Delta R_{\text{min}}(\mu, j)$ .

(F) Hadronic  $W$  reconstruction ( $jj_W$ ): among all dijet pairs, we select the pair with invariant mass closest to 80 GeV and label the jets by  $p_T$  as  $j_{W1}$  and  $j_{W2}$ . The input observables are

$$p_x(j_{W1}), p_y(j_{W1}), p_z(j_{W1}), E(j_{W1});$$

$$p_x(j_{W2}), p_y(j_{W2}), p_z(j_{W2}), E(j_{W2});$$

$$N_{\text{track}}(j_{W1}), N_{\text{track}}(j_{W2}); R_E(j_{W1}), R_E(j_{W2});$$

$$\Delta R(j_{W1}, j_{W2}), m(j_{W1} + j_{W2}).$$

(G) Transverse masses  $m_T$  [102]:  $m_T(\mu_1 + \cancel{E}_T)$  and  $m_T(\mu_2 + \cancel{E}_T)$ . Here, the transverse mass  $m_T$  of a visible system and the missing transverse momentum is defined as  $m_T^2 = (E_T^{\text{vis}} + \cancel{E}_T)^2 - |\vec{p}_T^{\text{vis}} + \vec{p}_T^{\text{miss}}|^2$ , where  $E_T^{\text{vis}} = \sqrt{|\vec{p}_T^{\text{vis}}|^2 + (m^{\text{vis}})^2}$  is the transverse energy of the visible system and  $\cancel{E}_T = |\vec{p}_T^{\text{miss}}|$  assumes a massless invisible system.

(H) Separations between the hadronic  $W$  candidate and each muon: we define  $\mu_a$  ( $\mu_b$ ) as the muon with the smaller (larger)  $\Delta R$  to the hadronic  $W$  candidate  $jj_W$ . The input observables are  $\Delta R(j_{W1} + j_{W2}, \mu_a)$  and  $\Delta R(j_{W1} + j_{W2}, \mu_b)$ .

(I) ALP-mass observables:  $m(j_{W1} + j_{W2} + \mu_a)$ ,  $m(j_{W1} + j_{W2} + \mu_b)$ , and  $m_T(j_{W1} + j_{W2} + \mu_a + \cancel{E}_T)$ ,  $m_T(j_{W1} + j_{W2} + \mu_b + \cancel{E}_T)$ .

(J) Off-shell  $W^{(*)}$  reconstruction:  $m_T(j_{W1} + j_{W2} + \mu_a + \mu_b + \cancel{E}_T)$ .

Details of  $N_{\text{track}}(j_i)$ ,  $R_E(j_i)$ ,  $R_{\text{grid}}(\mu_i)$ , and  $p_T^{\text{iso}}(\mu)$  can be found in Ref. [101]. The hadronic  $W$  candidate  $jj_W$  is reconstructed as described above. Appendix B.1 presents distributions of representative observables for the signal and background processes at the SppC/FCC-hh with  $\sqrt{s} = 100$  TeV, after applying the preselection criteria. For  $m_a \lesssim 500$  GeV, the endpoints of  $m(j_{W1} + j_{W2} + \mu_a)$  and  $m_T(j_{W1} + j_{W2} + \mu_a + \cancel{E}_T)$  track  $m_a$  closely. For larger  $m_a$ , the endpoint correlation of  $m_T(j_{W1} + j_{W2} + \mu_a + \cancel{E}_T)$  with  $m_a$  persists but becomes less pronounced.

Fig. 5 shows the BDT response distributions for the total SM background and the signal  $W^\pm a \rightarrow W^\pm W^\mp$  at the SppC/FCC-hh with  $\sqrt{s} = 100$  TeV, for  $m_a = 400$  GeV (left) and  $m_a = 900$  GeV (right). Appendix B.2 further shows the BDT response distributions for the signal and background processes at the SppC/FCC-hh with  $\sqrt{s} = 100$  TeV, after applying the preselection criteria, for representative values of  $m_a$ .

After the preselection, the BDT threshold is optimized independently at each  $m_a$  to maximize the statistical significance defined in Eq. (4.2). Appendix B.3 summarizes the preselection and BDT selection efficiencies for the signal and background processes at the SppC/FCC-hh with  $\sqrt{s} = 100$  TeV for various  $m_a$  benchmark points, where a “–” entry indicates that the yield is negligible for  $\mathcal{L} = 20 \text{ ab}^{-1}$ .

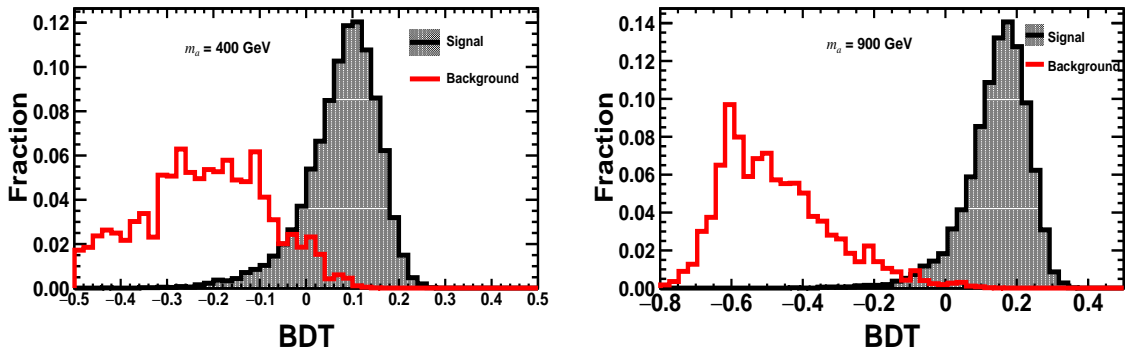


**Figure 5:** BDT response distributions for the total SM background and the signal  $W^\pm a(\rightarrow W^\pm W^\mp)$  at the SppC/FCC-hh with  $\sqrt{s} = 100$  TeV, for  $m_a = 400$  GeV (left) and  $m_a = 900$  GeV (right).

### 4.3 $W^+W^-jj$ final state

#### 4.3.1 Background processes

The signal targets two *oppositely charged, different-flavour leptons*, at least two jets, and moderate missing transverse momentum, i.e.  $e^\pm\mu^\mp + jj + \cancel{E}_T$ . In the  $e\mu$  channel, Drell–Yan contamination is strongly suppressed. The dominant backgrounds are well known to include diboson and top-quark production, as well as processes with nonprompt or misidentified leptons. Here, “nonprompt” denotes leptons from heavy-flavour decays in jets, hadron misidentification, or (for electrons) photon conversions. We group them by physics origin and by reducibility at detector level.

#### Irreducible (same visible final state)

- (a)  **$W^+W^-jj$  (QCD+EW).** Inclusive  $WW$  production in association with jets, dominated by  $q\bar{q} \rightarrow WW$  with additional QCD radiation [103]. After leptonic  $W$  decays, the visible final state coincides with the signal ( $e^\pm\mu^\mp + jj + \cancel{E}_T$ ).
- (b)  **$t\bar{t}$  (dileptonic).** When both  $W$  bosons decay leptonically,  $t\bar{t} \rightarrow \ell^+\nu\ell^-\bar{\nu} b\bar{b}$  can be indistinguishable from the signal up to global kinematics if  $b$  jets are not correctly tagged; it is therefore effectively irreducible in this channel.

#### Reducible (lost/misidentified objects)

- (c)  **$WZjj, ZZjj$ .** They contribute either when one prompt lepton is not reconstructed or fails identification/isolation, or when  $Z \rightarrow \tau\tau$  produces an  $e\mu$  pair.
- (d)  **$W^\pm jj$ .** Contributes via one prompt lepton from the  $W$  and one nonprompt or misidentified lepton (heavy-flavour decays, hadron misidentification, photon conversions).
- (e)  **$Zjj$ .** This background is strongly suppressed in the  $e\mu$  channel but remains nonzero through a misidentified lepton, a lost lepton plus a nonprompt lepton, or via  $Z \rightarrow \tau\tau \rightarrow e\mu + X$ .

The  $pp \rightarrow W^+W^-jj$  background is generated at matrix-element level with MadGraph5\_aMC@NLO, while the subsequent decays  $W \rightarrow \ell^\pm \nu_\ell$  ( $\ell = e, \mu$ ) and parton showering are modeled with PYTHIA 8.3. The  $t\bar{t}$ ,  $WZjj$ , and  $ZZjj$  samples are likewise produced with MadGraph5\_aMC@NLO and interfaced to PYTHIA 8.3, which handles all kinematically allowed  $W$ - and  $Z$ -boson decays. Single-boson processes  $W^\pm(\rightarrow \ell^\pm \nu_\ell)jj$  and  $Z(\rightarrow \ell^+\ell^-)jj$  with  $\ell = e, \mu$  are generated fully differentially in MadGraph5\_aMC@NLO, keeping the leptonic  $W$  and  $Z$  decays explicit in the matrix element.

### 4.3.2 Preselection

We target final states with two oppositely charged, different-flavour leptons, at least two jets, and moderate missing transverse momentum. Throughout, objects are ordered by transverse momentum, and the leading (subleading) jet is denoted by  $j_1$  ( $j_2$ ). The following preselection is applied to select the  $e^\pm \mu^\mp + jj + \cancel{E}_T$  final state and suppress backgrounds at the first stage:

- (i) Exactly two leptons:  $N(\ell) = 2$ ;
- (ii) Lepton transverse momenta:  $p_T(\ell) \geq 10$  GeV for both leptons;
- (iii) Different flavour: exactly one electron and one muon,  $N(e) = 1$  and  $N(\mu) = 1$ ;
- (iv) Opposite charge:  $Q(e) + Q(\mu) = 0$ ;
- (v) Jet multiplicity: at least two jets,  $N(j) \geq 2$ ;
- (vi) Leading-jet thresholds:  $p_T(j_1) \geq 30$  GeV and  $p_T(j_2) \geq 30$  GeV;
- (vii) Top-quark suppression: zero  $b$ -tagged jets,  $N(j_b) = 0$ .

This opposite-sign  $e\mu$  requirement strongly reduces Drell–Yan contamination, while the  $b$ -jet veto suppresses top-quark backgrounds, in line with LHC  $WW \rightarrow e^\pm \nu \mu^\mp \bar{\nu}$  measurements [103].

100 TeV $pp$	initial	(i)	(ii)	(iii)	(iv)	(v)	(vi)	(vii)
signal	$2.86 \times 10^8$	$1.89 \times 10^8$	$1.75 \times 10^8$	$8.74 \times 10^7$	$8.74 \times 10^7$	$8.41 \times 10^7$	$8.27 \times 10^7$	$6.11 \times 10^7$
$W^+(\rightarrow \ell^+ \nu) W^-(\rightarrow \ell^- \bar{\nu}) jj$	$1.38 \times 10^9$	$8.23 \times 10^8$	$7.35 \times 10^8$	$3.63 \times 10^8$	$3.63 \times 10^8$	$2.71 \times 10^8$	$2.38 \times 10^8$	$1.87 \times 10^8$
$WZjj$	$1.85 \times 10^{10}$	$1.34 \times 10^9$	$6.27 \times 10^8$	$5.05 \times 10^7$	$2.83 \times 10^7$	$2.48 \times 10^7$	$2.29 \times 10^7$	$1.70 \times 10^7$
$ZZjj$	$3.46 \times 10^9$	$3.23 \times 10^8$	$2.37 \times 10^8$	$3.76 \times 10^6$	$3.11 \times 10^6$	$2.78 \times 10^6$	$2.61 \times 10^6$	$1.80 \times 10^6$
$W^\pm(\rightarrow \ell^\pm \nu_\ell / \bar{\nu}_\ell) jj$	$3.50 \times 10^{12}$	$3.35 \times 10^{11}$	$8.77 \times 10^8$	$4.30 \times 10^8$	$2.34 \times 10^8$	$1.53 \times 10^8$	$1.22 \times 10^8$	$8.31 \times 10^7$
$Z(\rightarrow \ell^+\ell^-) jj$	$3.51 \times 10^{11}$	$2.06 \times 10^{11}$	$1.85 \times 10^{11}$	$2.28 \times 10^7$	$1.18 \times 10^7$	$9.30 \times 10^6$	$8.03 \times 10^6$	$5.64 \times 10^6$
$t\bar{t}$	$4.93 \times 10^{11}$	$4.23 \times 10^{10}$	$1.42 \times 10^{10}$	$7.03 \times 10^9$	$6.97 \times 10^9$	$6.45 \times 10^9$	$6.11 \times 10^9$	$6.36 \times 10^8$

**Table 4:** Event yields for the signal with benchmark  $m_a = 750$  GeV and for the background processes after sequentially applying preselection criteria (i)–(vii). Numbers correspond to a 100 TeV  $pp$  collider with  $\mathcal{L} = 20$  ab $^{-1}$ .

Table 4 shows the event yields after sequentially applying preselection criteria (i)–(vii) for the signal with benchmark  $m_a = 750$  GeV and for the background processes at the

SppC/FCC-hh with  $\sqrt{s} = 100$  TeV and  $\mathcal{L} = 20 \text{ ab}^{-1}$ . With the opposite-sign  $e\mu$  requirement, the large inclusive  $Wjj$  and  $Zjj$  rates are greatly reduced, while  $W^+W^-jj$  and  $t\bar{t}$  remain the leading backgrounds in the  $e\mu$  channel [103].

$m_a$ [GeV]	170	185	200	225	250	350
	$1.94 \times 10^{-1}$	$1.96 \times 10^{-1}$	$1.96 \times 10^{-1}$	$1.98 \times 10^{-1}$	$1.98 \times 10^{-1}$	$2.02 \times 10^{-1}$
$m_a$ [GeV]	750	1500	2500	4000	5500	7000
	$2.14 \times 10^{-1}$	$2.19 \times 10^{-1}$	$2.25 \times 10^{-1}$	$2.27 \times 10^{-1}$	$2.27 \times 10^{-1}$	$2.28 \times 10^{-1}$
background	$W^+(\rightarrow \ell^+\nu) W^-(\rightarrow \ell^-\bar{\nu}) jj$	$WZjj$	$ZZjj$	$W^\pm(\rightarrow \ell^\pm\nu_\ell) jj$	$Z(\rightarrow \ell^+\ell^-) jj$	$t\bar{t}$
	$1.36 \times 10^{-1}$	$9.19 \times 10^{-4}$	$5.19 \times 10^{-4}$	$2.37 \times 10^{-5}$	$1.61 \times 10^{-5}$	$1.29 \times 10^{-3}$

**Table 5:** Preselection efficiencies for the signals with different  $m_a$  values and for the background processes at a 100 TeV  $pp$  collider.

Table 5 summarizes the preselection efficiencies for the signals with different  $m_a$  values and for the background processes at a 100 TeV  $pp$  collider. As shown in this table, the  $Wjj$  and  $Zjj$  processes have the lowest preselection efficiencies because of the tight opposite-sign  $e\mu$  requirement. Diboson  $WZjj$  and  $ZZjj$  remain as subleading reducible backgrounds, primarily through lost leptons or  $\tau$  decays, while  $W^+W^-jj$  and  $t\bar{t}$  are effectively irreducible up to global kinematics; the latter is also strongly reduced by the  $b$ -tag veto.

#### 4.3.3 Multivariate analysis

After preselection, we employ a MVA to further discriminate signal from background. The input observables are:

- (i) Object kinematics: energy, transverse momentum, pseudorapidity, and azimuthal angle of the final-state objects,  $E(O)$ ,  $p_T(O)$ ,  $\eta(O)$ ,  $\phi(O)$  with  $O = \mu, e, j_1, j_2$ .
- (ii) Missing transverse momentum (magnitude and azimuthal angle):  $\cancel{E}_T$  and  $\phi(\cancel{E}_T)$ .
- (iii) Among all jet pairs, we identify the pair with the smallest angular separation, characterized by  $\Delta R(j, j')_{\min}$  and the corresponding dijet mass  $m(j + j')_{\min \Delta R}$ .
- (iv) Among all jet pairs, we also select the pair with the largest pseudorapidity separation,  $\Delta\eta(j, j')_{\max}$ , and its dijet mass  $m(j + j')_{\max \Delta\eta}$ .
- (v) The invariant mass of the two leading jets and the jet multiplicity:  $m(j_1 + j_2)$  and  $N(j)$ .
- (vi) Angular separations between key objects:  $\Delta R(j_1, j_2)$ ,  $\Delta\eta(j_1, j_2)$ ,  $\Delta R(e, \mu)$ ,  $\Delta R(\mu, j_1)$ ,  $\Delta R(\mu, j_2)$ ,  $\Delta R(e, j_1)$ ,  $\Delta R(e, j_2)$ .
- (vii) Transverse masses of leptons and  $\cancel{E}_T$ :  $m_T(\mu + \cancel{E}_T)$ ,  $m_T(e + \cancel{E}_T)$ , and  $m_T(\mu + e + \cancel{E}_T)$ .

Observables (iv)–(vi) exploit the VBF-like topology, characterized by two forward tagging jets, large  $\Delta\eta_{jj}$  and high  $m_{jj}$  with reduced central hadronic activity, while (iii) captures  $s$ -channel topologies where jets tend to be closer in phase space. This choice

follows standard LHC practices for VBF and dijet tagging. Observables (vii) are related to the kinematics of the decay  $a \rightarrow W^+W^- \rightarrow e^\pm\mu^\mp\nu\bar{\nu}$  in the  $e^\pm\mu^\mp + \cancel{E}_T$  final state. For completeness, Appendix C.1 displays distributions of representative observables for the signal and the six background processes at the SppC/FCC-hh with  $\sqrt{s} = 100$  TeV, assuming the benchmark  $m_a = 750$  GeV.

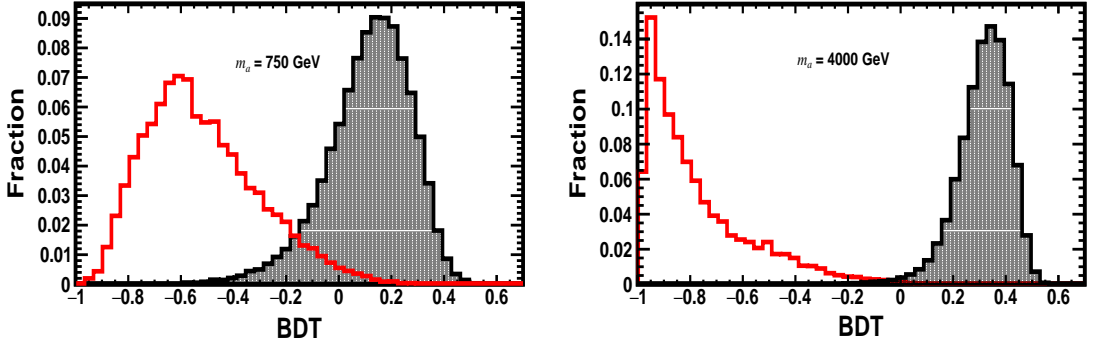


**Figure 6:** Distributions of BDT responses for the signal (black, shaded) and the total background (red) at  $\sqrt{s} = 100$  TeV, assuming  $m_a = 750$  GeV (left) and  $m_a = 4000$  GeV (right).

We implement the MVA using a BDT in the TMVA package integrated into ROOT, adopting the default BDT configuration for classification [97]. This setup is designed to maximize background rejection while retaining high signal efficiency. Fig. 6 shows the distributions of BDT responses for the signal and the total background at  $\sqrt{s} = 100$  TeV, assuming benchmarks  $m_a = 750$  GeV (left) and  $m_a = 4000$  GeV (right). Appendix C.2 shows BDT response distributions after applying the preselection criteria for the signal and background processes at the SppC/FCC-hh with  $\sqrt{s} = 100$  TeV for representative  $m_a$  values. As  $m_a$  increases, the underlying kinematics becomes more boosted and the separation between signal and background improves, as seen from the shift of the signal (background) distribution toward higher (lower) BDT scores.

Similar to previous analyses, the BDT threshold is then optimized independently at each  $m_a$  to maximize the statistical significance defined in Eq. (4.2). Appendix C.3 summarizes the selection efficiencies of the BDT cut for both signal and background processes at the SppC/FCC-hh with  $\sqrt{s} = 100$  TeV, assuming different ALP masses. Despite their large inclusive cross sections, the  $W^\pm(\rightarrow \ell^\pm\nu)jj$  and  $Z(\rightarrow \ell^+\ell^-)jj$  backgrounds are almost completely removed by the opposite-sign  $e\mu$  requirement and the multivariate selection, so they are omitted from the appendix table for brevity.

## 5 Results

Based on the preceding analyses, we present the discovery sensitivities for the signal at the SppC/FCC-hh with center-of-mass energy  $\sqrt{s} = 100$  TeV and integrated luminosity

$\mathcal{L} = 20 \text{ ab}^{-1}$ . Results are shown over the ALP mass range  $m_a \in [100, 7000] \text{ GeV}$ , both in terms of the coupling  $g_{aWW}$  and in terms of the model-independent fiducial quantity given by the signal production cross section times branching ratio,  $\sigma \times \text{Br}$ .

### 5.1 Sensitivities on $g_{aWW}$

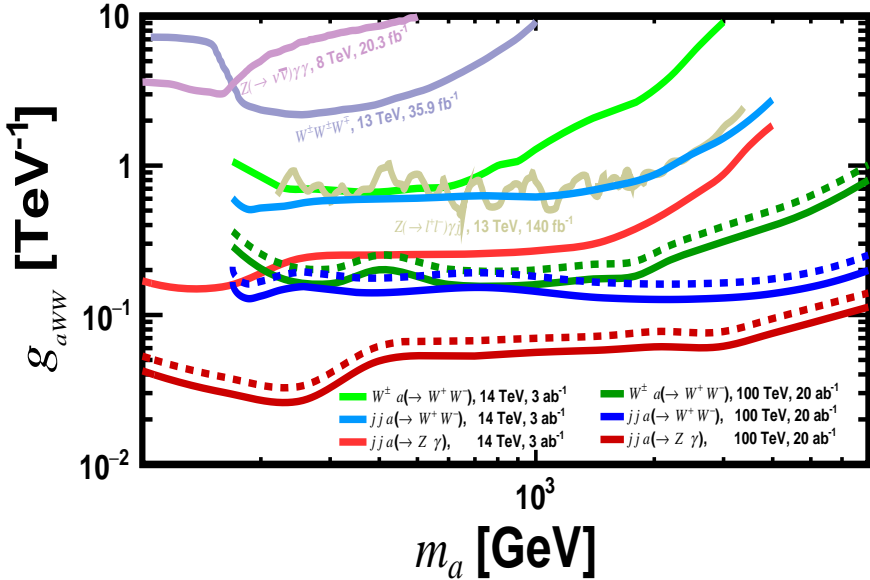


**Figure 7:** Projected discovery reach on the  $aWW$  coupling,  $g_{aWW}$ , for photophobic ALPs as a function of the ALP mass  $m_a$  in the range 100–7000 GeV at the SppC/FCC-hh with  $\sqrt{s} = 100 \text{ TeV}$  and  $\mathcal{L} = 20 \text{ ab}^{-1}$ . Solid (dashed) curves indicate  $2\sigma$  ( $5\sigma$ ) statistical significances. The projection assumes  $g_{a\gamma\gamma} = 0$  and a dedicated BDT optimization at each mass point; significances are statistical only. For comparison, we overlay existing 95% CL limits recast from the triboson channel  $pp \rightarrow Z(\rightarrow \nu\bar{\nu})\gamma\gamma$  at  $\sqrt{s} = 8 \text{ TeV}$  with  $20.3 \text{ fb}^{-1}$  [70], and from Run-2 analyses at  $\sqrt{s} = 13 \text{ TeV}$ :  $pp \rightarrow W^{\pm}W^{\pm}W^{\mp}$  with  $35.9 \text{ fb}^{-1}$  and  $pp \rightarrow Z(\rightarrow \ell^+\ell^-)\gamma jj$  with  $140 \text{ fb}^{-1}$  [76]. Also shown are HL-LHC ( $\sqrt{s} = 14 \text{ TeV}$ ,  $\mathcal{L} = 3 \text{ ab}^{-1}$ )  $2\sigma$  projections for  $pp \rightarrow jj a(\rightarrow Z\gamma)$  [77],  $pp \rightarrow W^{\pm}a(\rightarrow W^{\mp}W^{\pm})$  [78], and  $pp \rightarrow jj a(\rightarrow W^{\pm}W^{\mp})$  [79].

In Fig. 7, we summarize the projected discovery reach on the photophobic ALP–gauge coupling  $g_{aWW}$  as a function of the ALP mass  $m_a$ . The three sets of red, green and blue curves correspond to the signal topologies introduced in Fig. 1 at the SppC/FCC-hh ( $\sqrt{s} = 100 \text{ TeV}$ ,  $\mathcal{L} = 20 \text{ ab}^{-1}$ ): (I)  $pp \rightarrow jj a(\rightarrow Z\gamma)$ , (II)  $pp \rightarrow W^{\pm}a(\rightarrow W^{\mp}W^{\pm})$ , and (III)  $pp \rightarrow jj a(\rightarrow W^{\pm}W^{\mp})$ . For each topology we show both  $2\sigma$  and  $5\sigma$  discovery contours in the  $(m_a, g_{aWW})$  plane, obtained after the channel-specific BDT optimization described in Secs. 4.1, 4.2, and 4.3, and imposing the photophobic condition  $g_{a\gamma\gamma} = 0$ . The corresponding  $2\sigma$  HL-LHC projections at  $\sqrt{s} = 14 \text{ TeV}$  and  $\mathcal{L} = 3 \text{ ab}^{-1}$  from Refs. [77–79] are overlaid for direct comparison with the 100 TeV reach. In addition, the figure also displays, for reference,

existing 95% CL limits obtained by recasting LHC measurements: the Run-1 triboson channel  $pp \rightarrow Z(\rightarrow \nu\bar{\nu})\gamma\gamma$  at  $\sqrt{s} = 8$  TeV with  $20.3 \text{ fb}^{-1}$  [70], and the Run-2 measurements of  $pp \rightarrow W^\pm W^\pm W^\mp$  ( $35.9 \text{ fb}^{-1}$ ) and  $pp \rightarrow Z(\rightarrow \ell^+\ell^-)\gamma jj$  ( $140 \text{ fb}^{-1}$ ) at  $\sqrt{s} = 13$  TeV [76].

Comparing the three 100 TeV curves in Fig. 7, one finds a clear hierarchy among the signal topologies. Over the full mass range, the  $jj a(\rightarrow Z\gamma)$  channel (I) provides the best reach in  $g_{aWW}$ . This final state combines a fully reconstructible  $m(\ell^+ + \ell^- + \gamma)$  resonance, excellent photon and lepton energy resolution, and relatively small irreducible backgrounds, which together permit tight BDT selections with only modest signal loss. Among the two  $WW$  modes, the  $jj a(\rightarrow W^+W^-)$  channel (III) overtakes the  $W^\pm a(\rightarrow W^+W^-)$  channel (II) once  $m_a \gtrsim \mathcal{O}(1 \text{ TeV})$ . The origin is twofold. First, channel (III) receives contributions from both  $s$ -channel vector-boson exchange and genuine VBF topologies, so at high mass it benefits from the rapid growth of the electroweak vector-boson luminosity and the large phase space for two energetic forward jets. By contrast,  $pp \rightarrow W^\pm a$  in channel (II) proceeds purely through an  $s$ -channel configuration and its cross section drops more steeply with  $m_a$ . Second, both  $WW$  channels are intrinsically less clean than  $Z\gamma$ : leptonic  $W$  decays introduce sizeable genuine  $\cancel{E}_T$ , large SM  $WW$  and  $t\bar{t}$  backgrounds, and no fully reconstructible resonance. Even though  $\text{Br}(a \rightarrow W^+W^-)$  exceeds  $\text{Br}(a \rightarrow Z\gamma)$  in the photophobic limit, these effects weaken the net reach in  $g_{aWW}$ . In summary, at 100 TeV the  $jj a(\rightarrow Z\gamma)$  channel (I) sets the benchmark sensitivity; the  $jj a(\rightarrow W^+W^-)$  channel (III) provides the next-best, and increasingly competitive, reach at high masses thanks to its VBF component; and the  $W^\pm a(\rightarrow W^+W^-)$  channel (II), while statistically less powerful especially at high mass, probes the same coupling in a complementary production mode and final state.

A comparison between the SppC/FCC-hh ( $\sqrt{s} = 100 \text{ TeV}, \mathcal{L} = 20 \text{ ab}^{-1}$ ) projections and the HL-LHC ( $\sqrt{s} = 14 \text{ TeV}, \mathcal{L} = 3 \text{ ab}^{-1}$ ) results for the same three final states highlights the combined impact of higher energy and luminosity. In all channels the gain is modest at low  $m_a$ , where production is dominated by relatively soft partons already abundant at the LHC. Once  $m_a$  enters the TeV regime, however, the much larger partonic centre-of-mass energy and enhanced electroweak boson luminosities at 100 TeV increase the signal cross sections by orders of magnitude. This translates into roughly an order-of-magnitude improvement in the reachable  $g_{aWW}$  values compared to the HL-LHC, and extends the mass reach by several TeV. The effect is most pronounced in the VBF-assisted channels (I) and (III), whose cross sections grow with energy, while the purely  $s$ -channel tri- $W$  mode (II) benefits mainly from the larger luminosity but still gains significantly in the multi-TeV mass range.

Despite their weaker raw sensitivity, the tri- $W$  channel (II) and the  $jj a(\rightarrow W^+W^-)$  channel (III) provide essential information that is not redundant with the  $jj a(\rightarrow Z\gamma)$  channel (I). Channel (II) probes  $pp \rightarrow W^\pm a$  in a purely  $s$ -channel configuration with a very clean same-sign dilepton signature; its background composition, trigger strategy and dominant systematics are qualitatively different from those of the  $Z\gamma jj$  analysis. Channel (III), by contrast, probes the same  $aWW$  vertex in a mixed  $s$ +VBF configuration, where two forward/backward tagging jets and large  $|\Delta\eta_{jj}|$  make it particularly sensitive to the Lorentz and CP structure of the  $aWW$  operator. Both  $WW$  channels directly test

the  $aWW$  coupling via  $a \rightarrow W^+W^-$ , whereas  $jj\,a(\rightarrow Z\gamma)$  constrains  $aZ\gamma$ . A combined analysis of all three therefore overconstraints the photophobic relations  $g_{aZ\gamma} = t_\theta g_{aWW}$  and  $g_{aZZ} = (1 - t_\theta^2) g_{aWW}$ , provides powerful cross-checks against channel-specific systematics, and offers a robust basis for global fits. In this sense, the three topologies are not merely alternative search modes but together form a coherent programme to test the gauge structure and high-energy behaviour of photophobic ALP scenarios.

## 5.2 Sensitivities on production cross sections

To facilitate reinterpretations beyond the photophobic benchmark, we also present model-independent discovery thresholds on the inclusive rate  $\sigma \times \text{Br}$  for each signal topology at the SppC/FCC-hh ( $\sqrt{s} = 100$  TeV,  $\mathcal{L} = 20 \text{ ab}^{-1}$ ). Figs. 8–10 show the minimum  $\sigma \times \text{Br}$  required for a  $2\sigma$  (solid) or  $5\sigma$  (dashed) excess after the full preselection and BDT-based analysis. In all three channels, the reach generally improves (smaller  $\sigma \times \text{Br}$ ) as  $m_a$  increases, because the selected SM background falls rapidly in the high-mass region and the signal kinematics become more distinctive, enabling tighter multivariate selections at nearly constant signal efficiency.

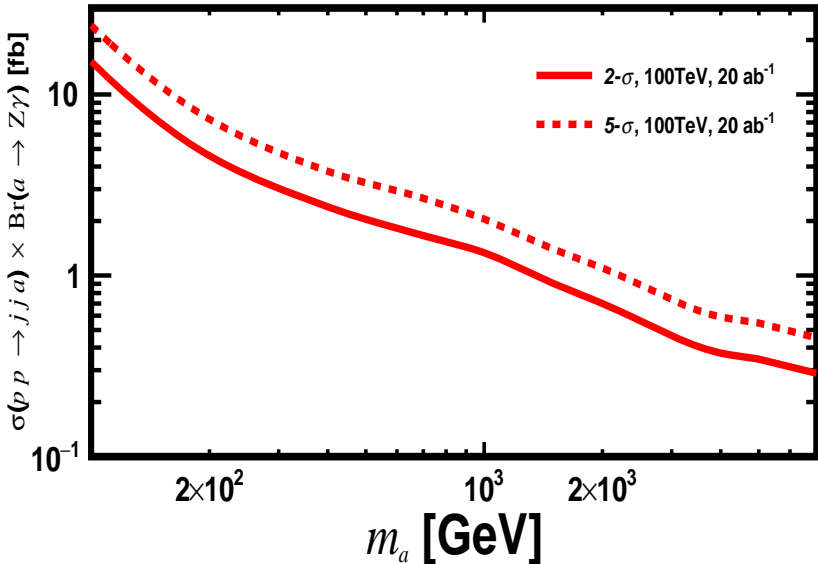


**Figure 8:** Discovery sensitivities on the production cross section  $\sigma(pp \rightarrow jj\,a)$  times the branching ratio  $\text{Br}(a \rightarrow Z\gamma)$  as a function of  $m_a$  from 100 to 7000 GeV at the SppC/FCC-hh with  $\sqrt{s} = 100$  TeV and  $\mathcal{L} = 20 \text{ ab}^{-1}$ . The solid (dashed) curves correspond to  $2\sigma$  ( $5\sigma$ ) significance.

In the  $jj\,a(\rightarrow Z\gamma)$  channel (I), Fig. 8 reports the discovery reach on  $\sigma(pp \rightarrow jj\,a) \times \text{Br}(a \rightarrow Z\gamma)$ . The required rate drops from  $\mathcal{O}(10)$  fb at  $m_a \sim 100$  GeV to the sub-fb level toward the multi-TeV regime. This strong performance is driven by the clean experimental signature and, crucially, by the fully reconstructible  $m(\ell^+ + \ell^- + \gamma)$  resonance, which

effectively localizes the search to a narrow mass region where the continuum background is both small and rapidly falling.

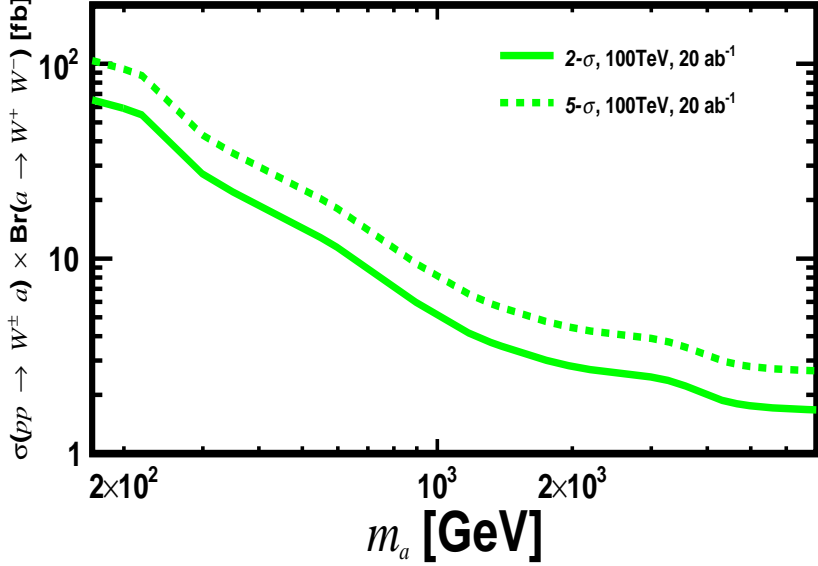


**Figure 9:** Discovery sensitivities on  $\sigma(pp \rightarrow W^\pm a) \times \text{Br}(a \rightarrow W^+W^-)$  in the mass range 170–7000 GeV at the SppC/FCC-hh with  $\sqrt{s} = 100$  TeV and  $\mathcal{L} = 20 \text{ ab}^{-1}$ . The solid (dashed) curves correspond to  $2\sigma$  ( $5\sigma$ ) significance.

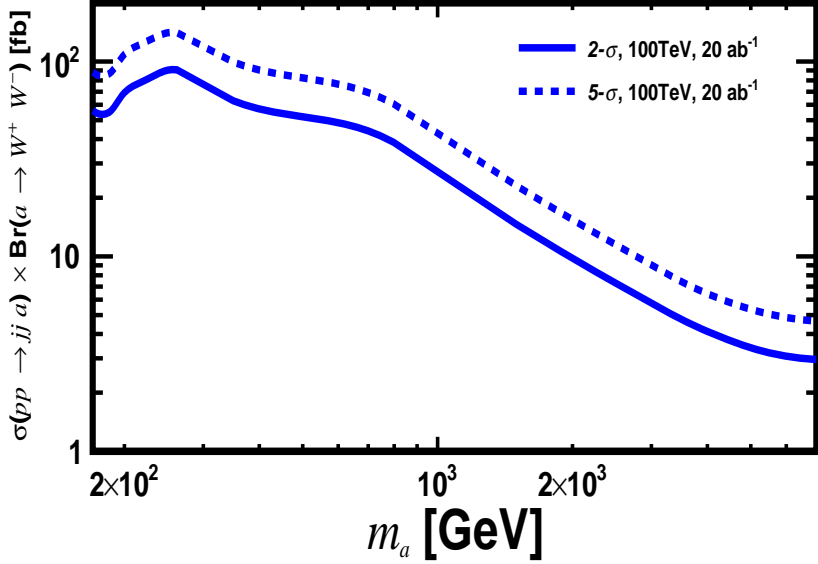


**Figure 10:** Discovery sensitivities on  $\sigma(pp \rightarrow jj a) \times \text{Br}(a \rightarrow W^+W^-)$  in the mass range 170–7000 GeV at the SppC/FCC-hh with  $\sqrt{s} = 100$  TeV and  $\mathcal{L} = 20 \text{ ab}^{-1}$ . The solid (dashed) curves correspond to  $2\sigma$  ( $5\sigma$ ) significance.

For the associated-production  $W^\pm a(\rightarrow W^+W^-)$  channel (II), Fig. 9 shows the reach on  $\sigma(pp \rightarrow W^\pm a) \times \text{Br}(a \rightarrow W^+W^-)$ . The sensitivity improves from  $\mathcal{O}(10^2)$  fb near threshold to  $\mathcal{O}(1)$  fb at multi-TeV masses. Although this channel does not admit a fully reconstructed ALP mass peak due to neutrinos, it benefits from a very rare same-sign dilepton signature, which suppresses many SM backgrounds already at the object-selection level; the remaining backgrounds also become increasingly phase-space limited at large  $m_a$ , yielding good high-mass reach in  $\sigma \times \text{Br}$ .

Finally, for the  $jj a(\rightarrow W^+W^-)$  channel (III), Fig. 10 presents the reach on  $\sigma(pp \rightarrow jj a) \times \text{Br}(a \rightarrow W^+W^-)$ . At low masses the required rate is comparatively larger, reflecting the intrinsically less constrained kinematics of dileptonic  $WW$  decays (genuine  $\cancel{E}_T$  and no narrow fully reconstructible resonance) and the sizeable irreducible backgrounds from SM  $WW$  and  $t\bar{t}$ . The reach nonetheless strengthens rapidly with increasing  $m_a$ , reaching a few-fb level in the multi-TeV regime, consistent with both the falling background and the increasingly boosted/VBF-like event structure that enhances multivariate separation power.

These  $\sigma \times \text{Br}$  curves can be directly reused to constrain other new-physics scenarios that populate the same reconstructed final states and have comparable acceptances. Concretely, for a model predicting a narrow resonance  $X$  in one of the three topologies of Fig. 1, discovery is expected once  $\sigma(pp \rightarrow X + \dots) \times \text{Br}(X \rightarrow \text{final state})$  exceeds the corresponding curve, up to an acceptance/efficiency correction if the kinematics differ significantly from those of the benchmark ALP simulation.

## 6 Conclusion

Searches for axion-like particles (ALPs) at colliders are often driven by diphoton signatures, which tightly constrain the effective ALP–photon coupling  $g_{a\gamma\gamma}$ . This motivates “photophobic” scenarios in which the diphoton coupling is suppressed, while electroweak couplings remain sizable. In this work we therefore set  $g_{a\gamma\gamma} = 0$  and study heavy photophobic ALPs at a future 100 TeV proton–proton collider (SppC/FCC-hh) with an integrated luminosity of  $\mathcal{L} = 20 \text{ ab}^{-1}$ .

We consider ALP production through electroweak boson exchange, including both  $s$ -channel and VBF-like topologies when applicable, and analyze three complementary discovery channels (cf. Fig. 1): (I)  $pp \rightarrow jj a(\rightarrow Z\gamma)$  with  $Z \rightarrow \ell^+\ell^-$  ( $\ell = e, \mu$ ); (II)  $pp \rightarrow W^\pm a(\rightarrow W^+W^-)$  with a same-sign dimuon signature plus a hadronic  $W$ ; and (III)  $pp \rightarrow jj a(\rightarrow W^+W^-)$  with opposite-sign, different-flavor dilepton  $e^\pm\mu^\mp$  in the final state. Signal and background events are generated with MadGraph5\_aMC@NLO and showered with PYTHIA 8, followed by a Delphes detector simulation. Each analysis applies a dedicated preselection and then a TMVA-based BDT using channel-specific kinematic observables; for every ALP-mass hypothesis, the BDT threshold is optimized to maximize the statistical discovery significance.

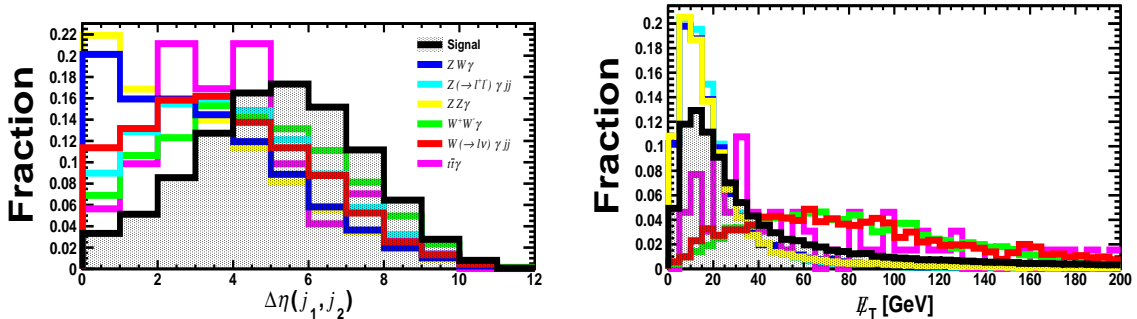
Our main results are the projected discovery reaches in the  $(m_a, g_{aWW})$  plane and the corresponding model-independent thresholds in  $\sigma \times \text{Br}$ . At  $\sqrt{s} = 100$  TeV, the  $jj a(\rightarrow$

$Z\gamma$ ) channel (I) gives the strongest reach across the full mass range, driven by a fully reconstructible  $m(\ell^+ + \ell^- + \gamma)$  resonance and comparatively small irreducible backgrounds. The two  $WW$  modes are intrinsically less clean—neutrinos induce genuine  $\cancel{E}_T$  and prevent a narrow mass reconstruction, and SM  $WW$  and  $t\bar{t}$  backgrounds are sizable—but they are far from auxiliary. Channel (II),  $pp \rightarrow W^\pm a(\rightarrow W^+W^-)$ , is a *pure s-channel* probe with a very clean same-sign dilepton signature and largely independent background composition and systematics, providing a robust cross-check in a qualitatively different production environment. Channel (III),  $pp \rightarrow jj a(\rightarrow W^+W^-)$ , receives both *s*-channel and VBF-like contributions; at high  $m_a$  it becomes increasingly competitive thanks to the forward-tagging-jet topology, the growing importance of vector-boson luminosities at 100 TeV, and its sensitivity to the Lorentz/CP structure of the  $aWW$  operator through dijet correlations. Taken together, the three channels form an overconstrained test of the photophobic ALP hypothesis: channel (I) maximizes discovery potential, while channels (II) and (III) directly interrogate  $a \rightarrow W^+W^-$  in complementary production regimes, enabling stringent internal consistency tests of the electroweak coupling pattern and providing essential validation and, if an excess emerges, enabling characterization of a potential signal.

Finally, by presenting the discovery thresholds on  $\sigma(pp \rightarrow jj a) \times \text{Br}(a \rightarrow Z\gamma)$ ,  $\sigma(pp \rightarrow W^\pm a) \times \text{Br}(a \rightarrow W^+W^-)$ , and  $\sigma(pp \rightarrow jj a) \times \text{Br}(a \rightarrow W^+W^-)$ , we enable straightforward reinterpretations for other new-physics models that populate the same reconstructed final states. Overall, our study shows that a 100 TeV collider would substantially extend the discovery coverage for photophobic ALPs into the multi-TeV mass regime and significantly improve upon HL-LHC projections, while a combined program across the three signal channels (I)–(III) provides both sensitivity and resilience against channel-specific limitations.

## A Details of the $Z\gamma jj$ analyses

### A.1 Distributions of representative observables



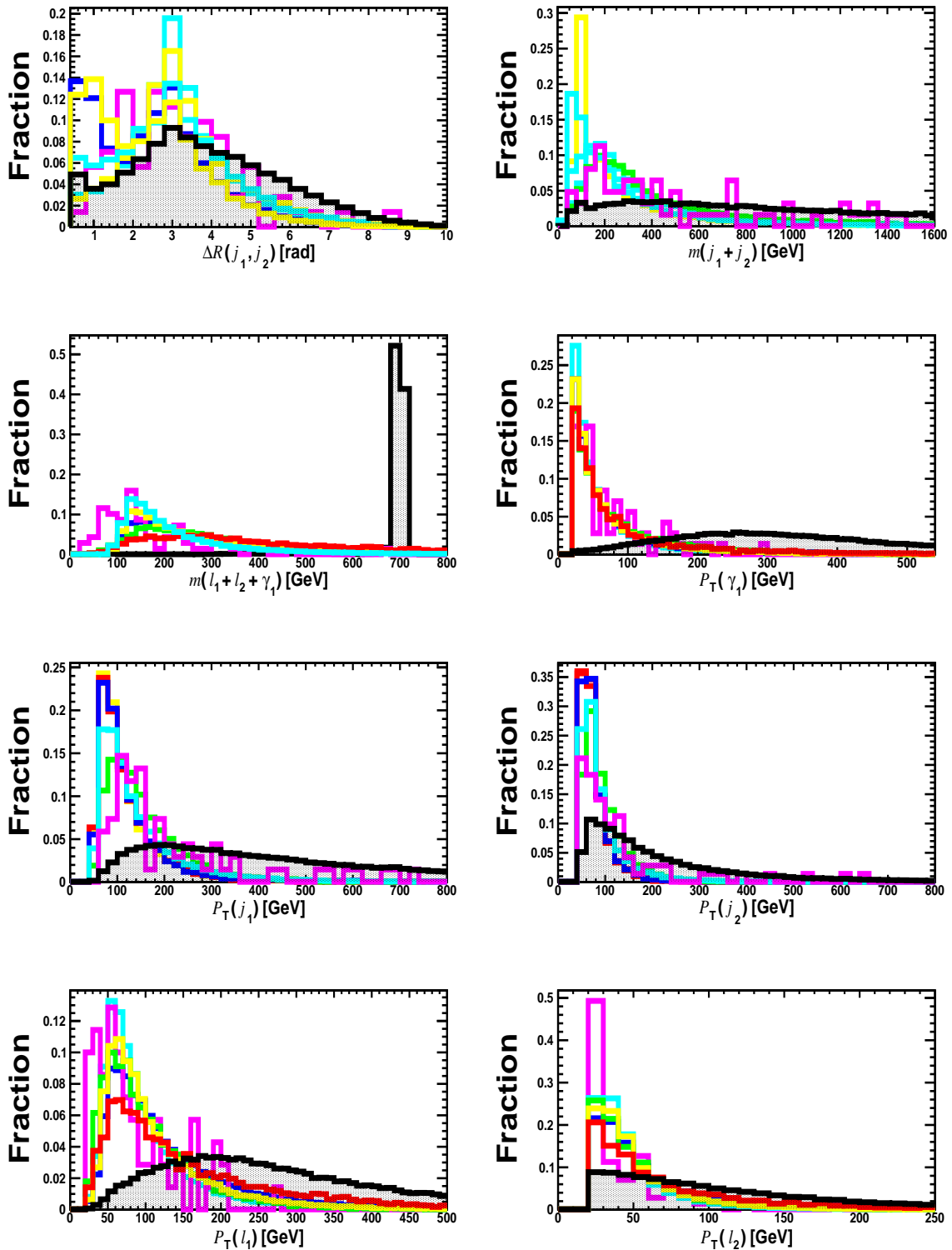


**Figure 11:** Distributions of representative observables for the signal with benchmark  $m_a = 700$  GeV and for the six background processes at the SppC/FCC-hh with  $\sqrt{s} = 100$  TeV, after the preselection criteria are applied.

## A.2 Distributions of BDT responses

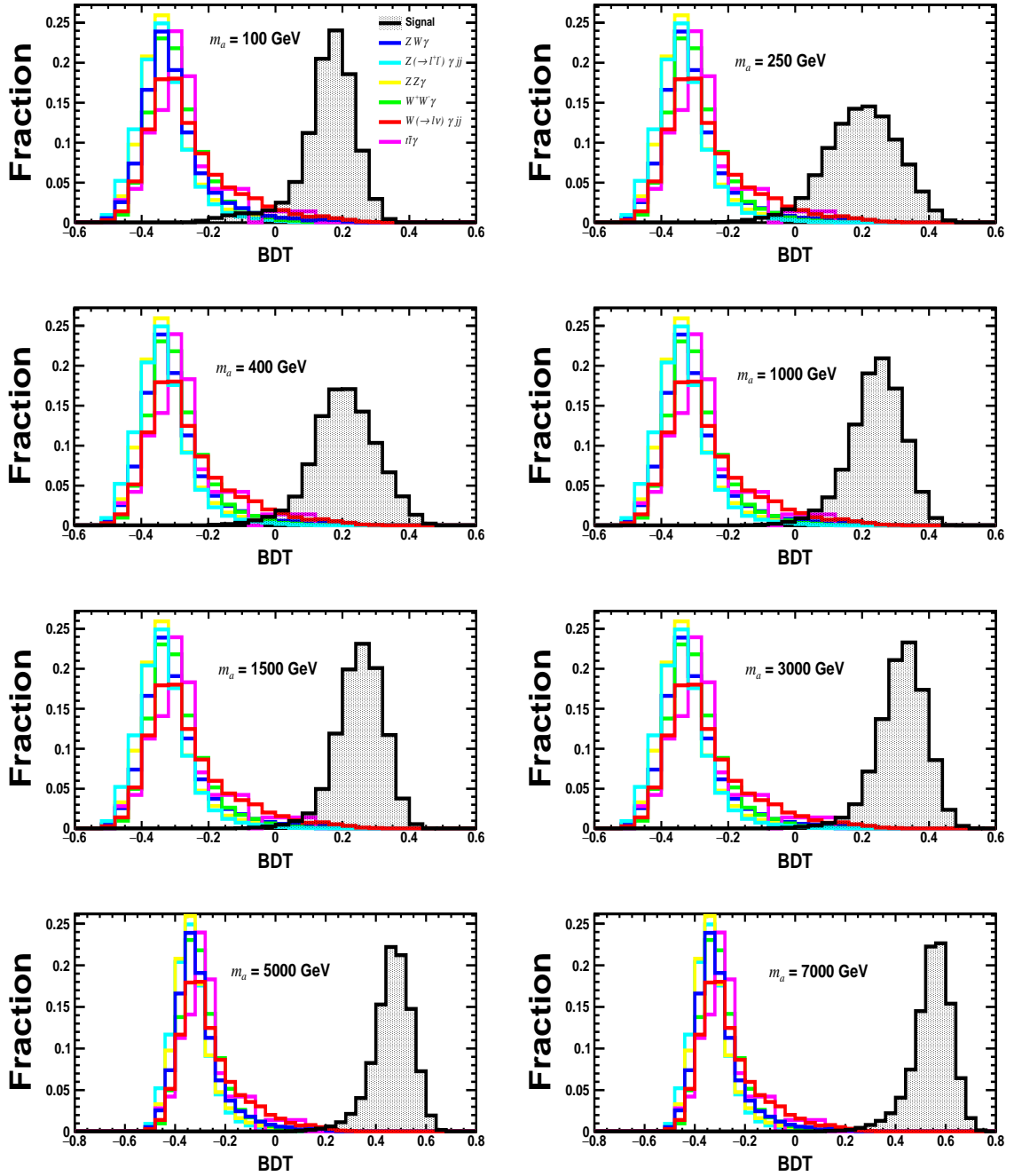


**Figure 12:** Distributions of BDT responses for the signal (black, shaded) and the six background processes at the SppC/FCC-hh with  $\sqrt{s} = 100$  TeV, assuming different  $m_a$  values.

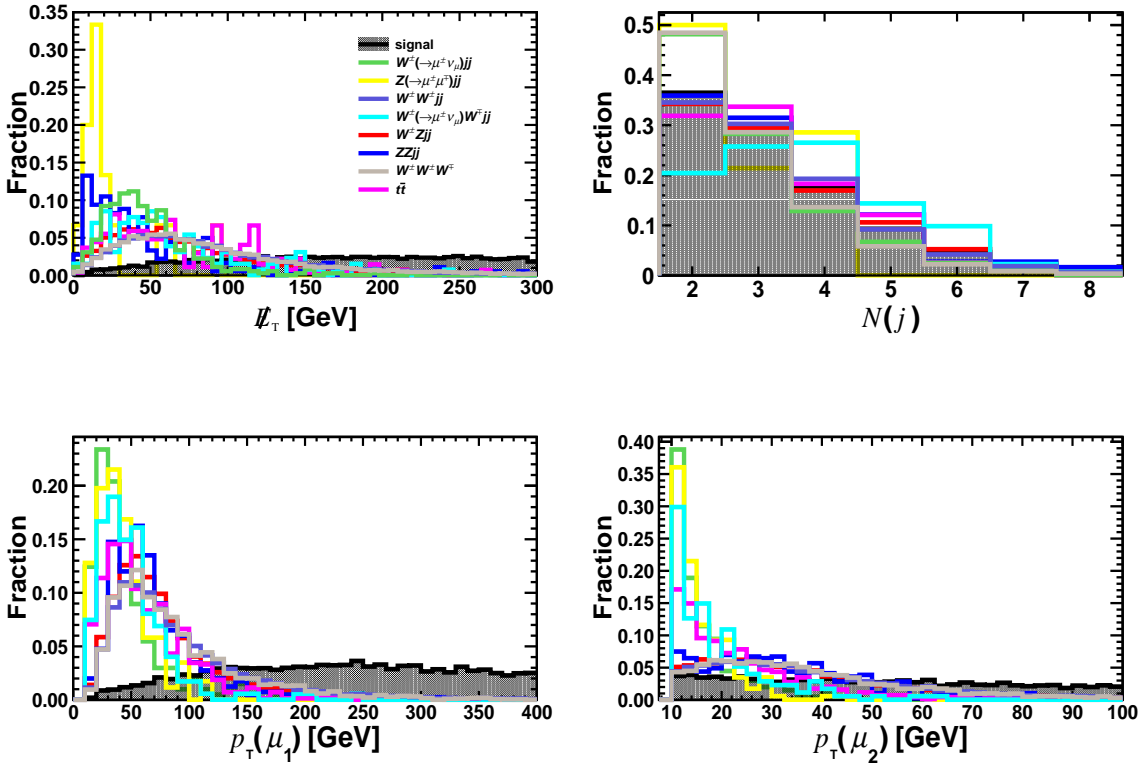
## A.3 BDT selection efficiencies

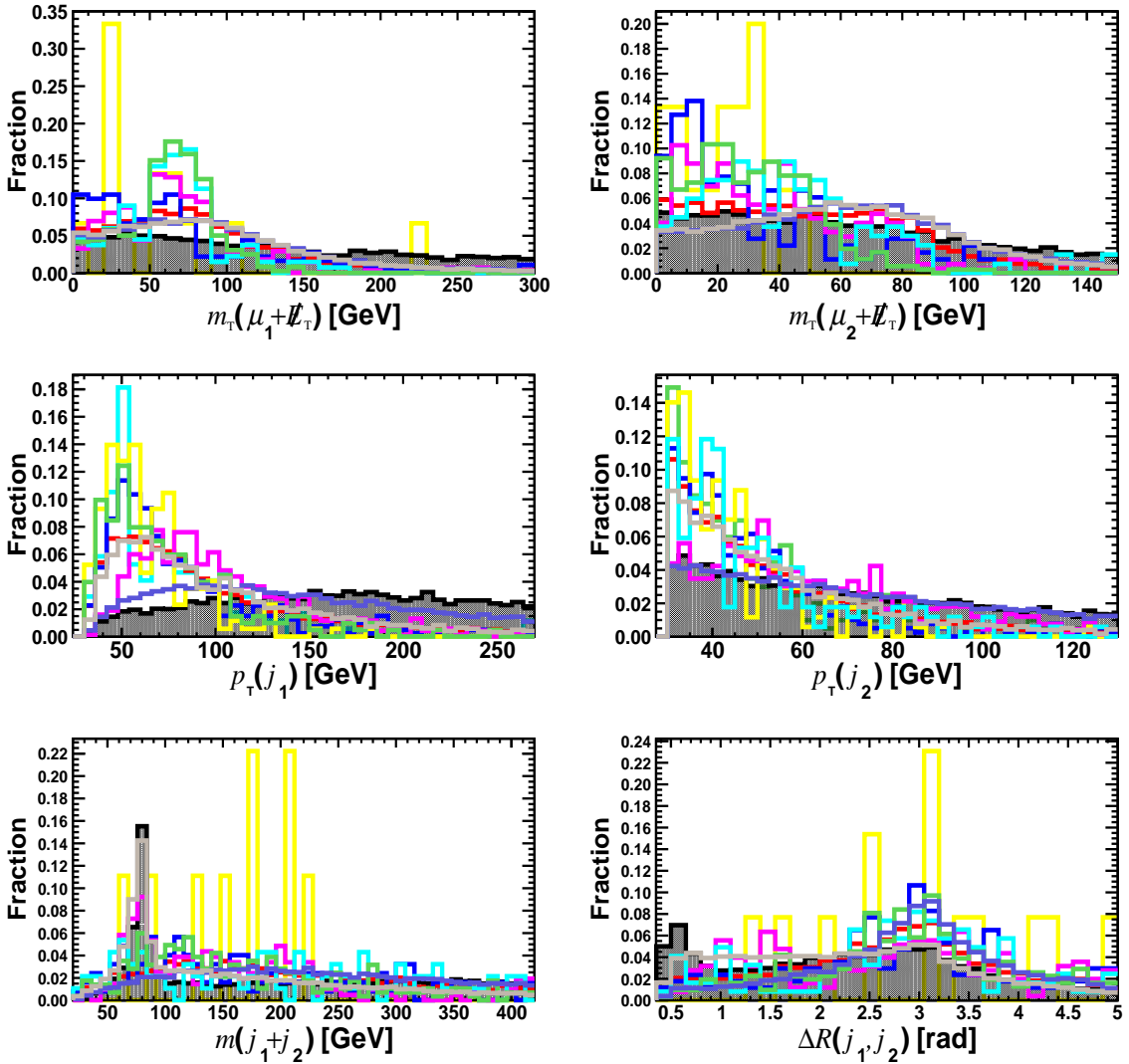
$m_a$ [GeV]	BDT	signal	$ZW\gamma$	$Z(\rightarrow \ell^+\ell^-)\gamma jj$	$ZZ\gamma$	$W^+W^-\gamma$	$W(\rightarrow \ell\nu)\gamma jj$	$t\bar{t}\gamma$
100	0.108	$7.99 \times 10^{-1}$	$3.89 \times 10^{-3}$	$3.14 \times 10^{-3}$	$4.64 \times 10^{-3}$	$5.54 \times 10^{-4}$	—	$2.94 \times 10^{-4}$
165	0.121	$7.47 \times 10^{-1}$	$3.44 \times 10^{-3}$	$2.96 \times 10^{-3}$	$5.74 \times 10^{-3}$	$2.22 \times 10^{-3}$	—	$3.82 \times 10^{-3}$
400	0.149	$7.49 \times 10^{-1}$	$1.95 \times 10^{-3}$	$1.18 \times 10^{-3}$	$2.36 \times 10^{-3}$	$4.46 \times 10^{-3}$	—	$6.32 \times 10^{-3}$
700	0.140	$8.88 \times 10^{-1}$	$2.40 \times 10^{-3}$	$1.10 \times 10^{-3}$	$1.86 \times 10^{-3}$	$8.04 \times 10^{-3}$	—	$4.71 \times 10^{-3}$
1000	0.147	$8.84 \times 10^{-1}$	$3.05 \times 10^{-3}$	$7.73 \times 10^{-4}$	$1.56 \times 10^{-3}$	$8.04 \times 10^{-3}$	—	$2.79 \times 10^{-3}$
1500	0.200	$8.35 \times 10^{-1}$	$1.62 \times 10^{-3}$	$3.24 \times 10^{-4}$	$9.51 \times 10^{-4}$	$7.48 \times 10^{-3}$	—	$1.03 \times 10^{-3}$
2000	0.190	$9.10 \times 10^{-1}$	$2.72 \times 10^{-3}$	$2.51 \times 10^{-4}$	$1.18 \times 10^{-3}$	$6.93 \times 10^{-3}$	—	$7.36 \times 10^{-4}$
4000	0.200	$9.88 \times 10^{-1}$	$1.75 \times 10^{-3}$	$1.25 \times 10^{-4}$	$5.33 \times 10^{-4}$	$3.88 \times 10^{-3}$	—	—
5000	0.225	$9.88 \times 10^{-1}$	$1.04 \times 10^{-3}$	$6.48 \times 10^{-5}$	$3.42 \times 10^{-4}$	$2.22 \times 10^{-3}$	—	—
7000	0.199	$9.88 \times 10^{-1}$	$6.48 \times 10^{-4}$	$5.26 \times 10^{-5}$	$2.66 \times 10^{-4}$	$1.38 \times 10^{-3}$	—	—

**Table 6:** Selection efficiencies of the BDT cut for both signal and background processes at the SppC/FCC-hh with  $\sqrt{s} = 100$  TeV for different  $m_a$  values. The second column gives the lower threshold of the BDT response; “—” indicates that the yield becomes negligible with  $\mathcal{L} = 20$  ab $^{-1}$ .

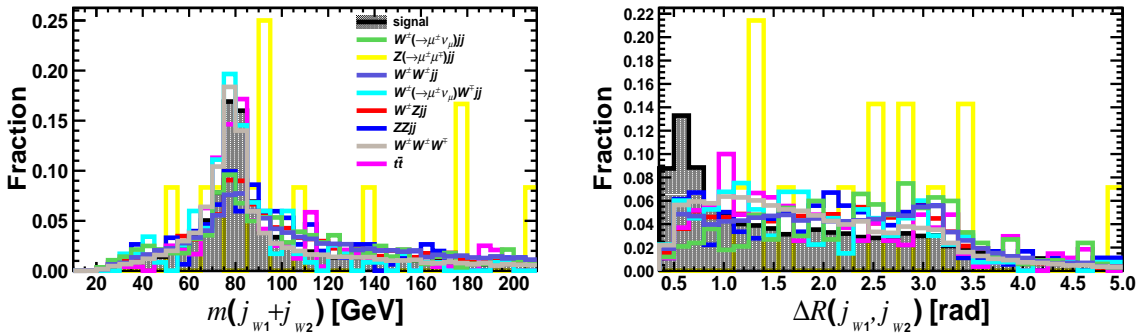
## B Details of the $W^\pm W^\pm W^\mp$ analyses

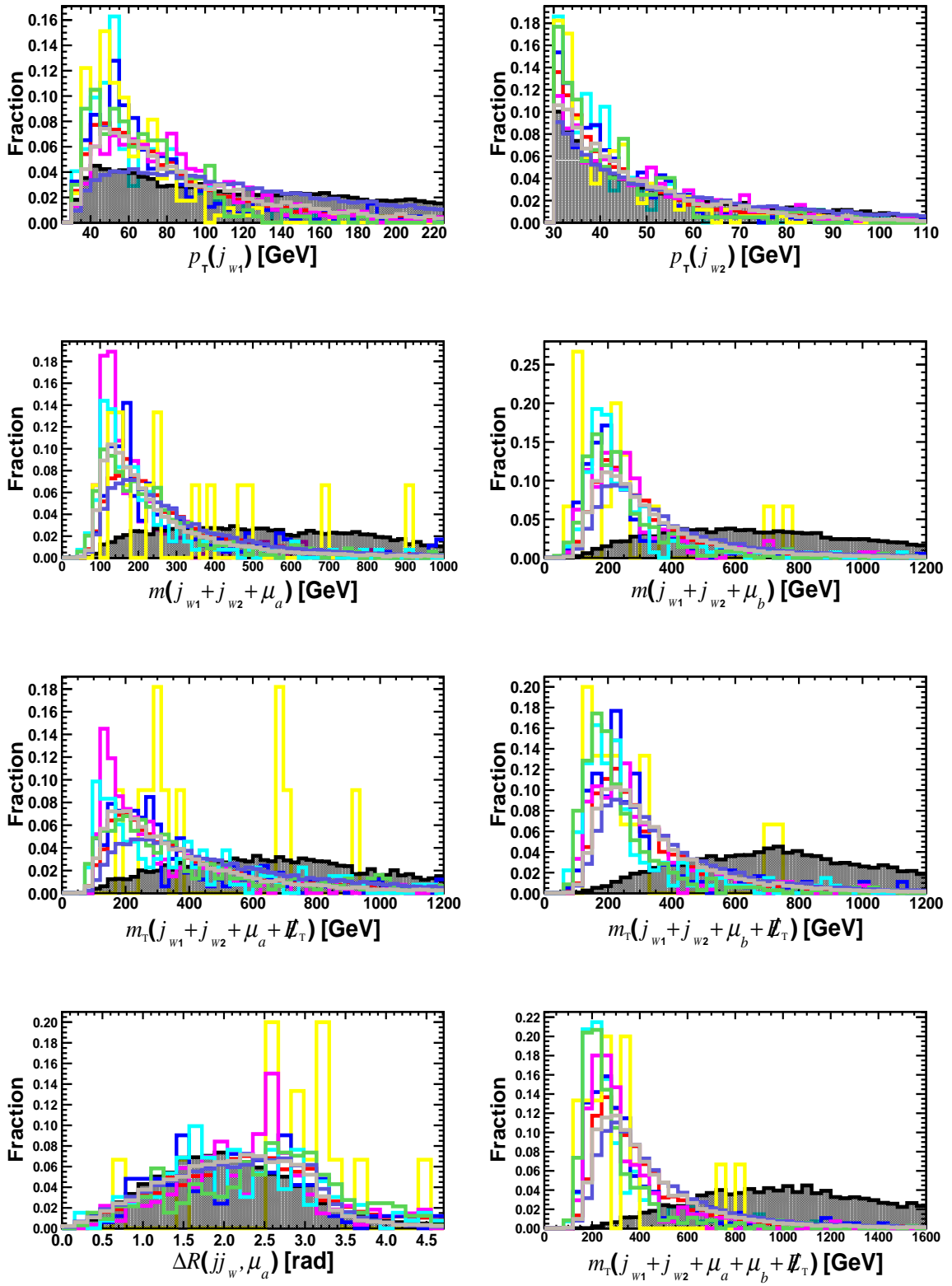
### B.1 Distributions of representative observables



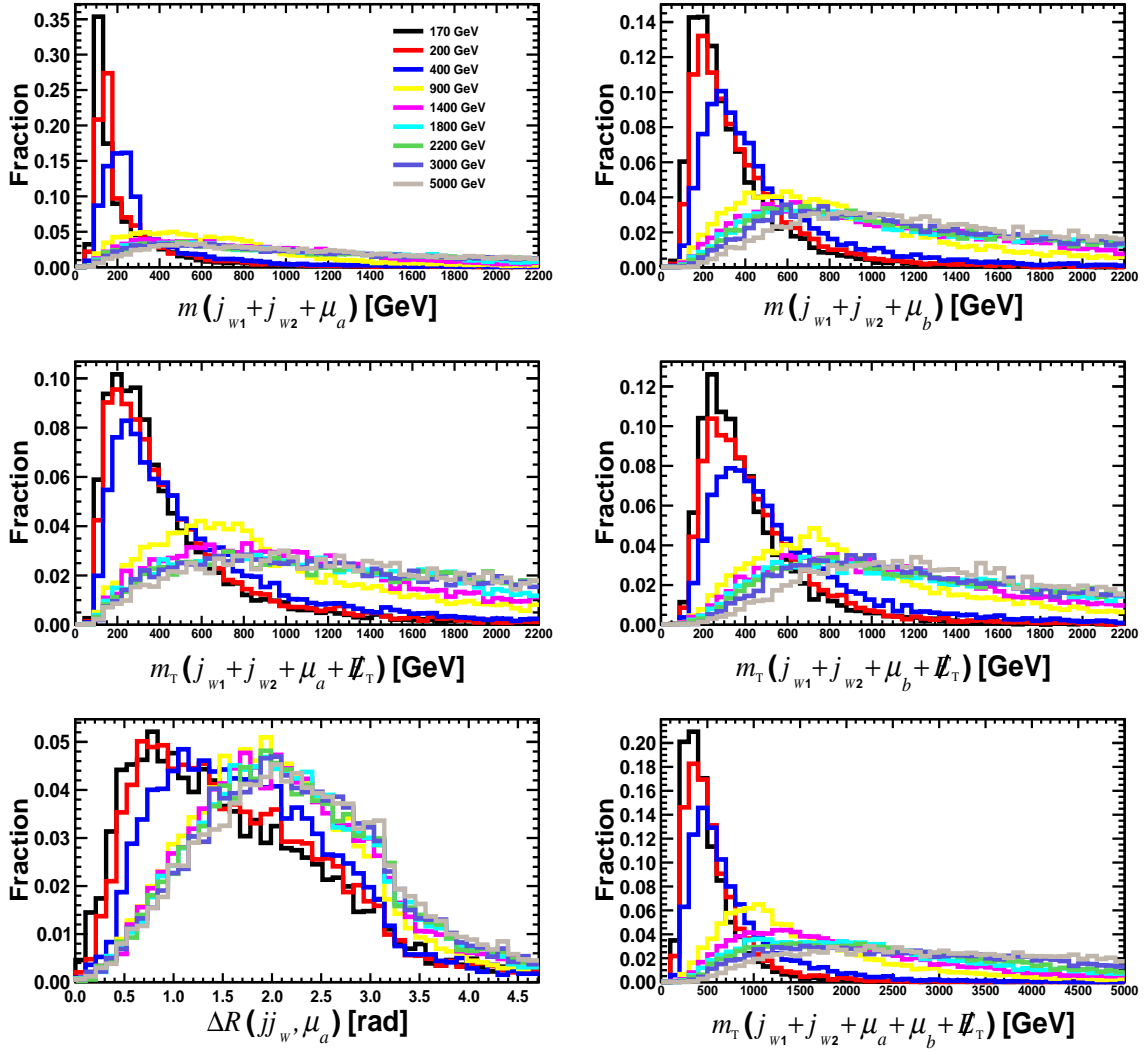


**Figure 13:** Distributions of kinematic observables for  $\cancel{E}_T$ ,  $N(j)$ ,  $\mu_1$ ,  $\mu_2$ ,  $j_1$ , and  $j_2$  after applying the preselection criteria for the signal (black, shaded) and background processes at the SppC/FCC-hh with  $\sqrt{s} = 100$  TeV, assuming the benchmark  $m_a = 900$  GeV.



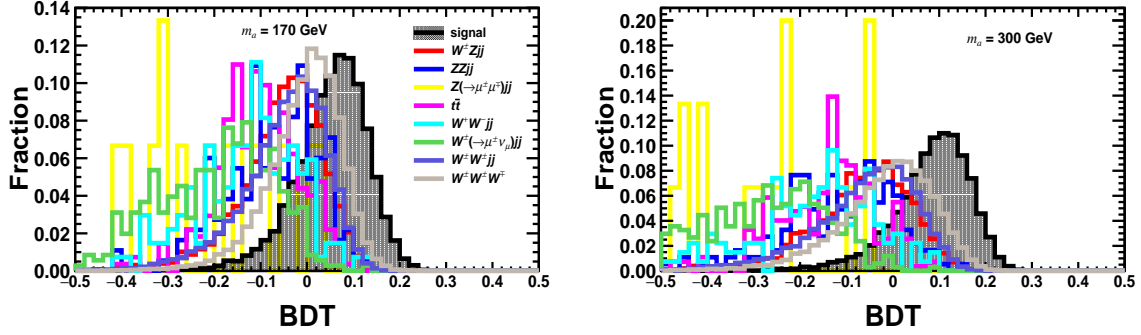


**Figure 14:** Same as Fig. 13, but for  $j_{w1}$ ,  $j_{w2}$ , and observables related to the reconstruction of the ALP mass and the off-shell  $W^{(*)\pm}$  boson, assuming the benchmark  $m_a = 900$  GeV.



**Figure 15:** Distributions of the observables related to the reconstruction of the ALP mass and the off-shell  $W^{(*)\pm}$  boson, for the signal only, assuming different  $m_a$  values.

## B.2 Distributions of BDT responses



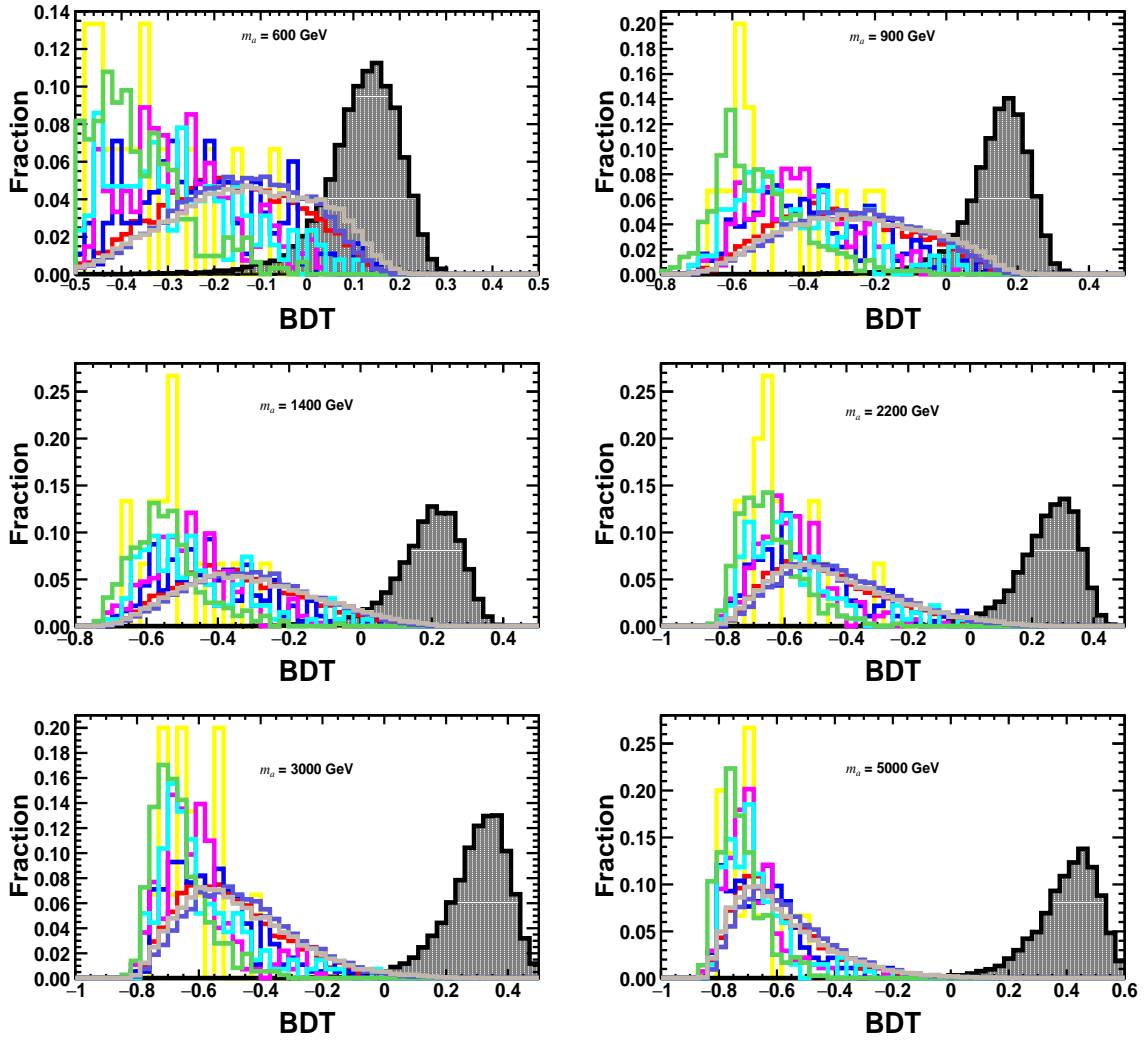


**Figure 16:** Distributions of BDT responses after applying the preselection criteria for the signal (black, shaded) and background processes at the SppC/FCC-hh with  $\sqrt{s} = 100$  TeV for representative  $m_a$  values.

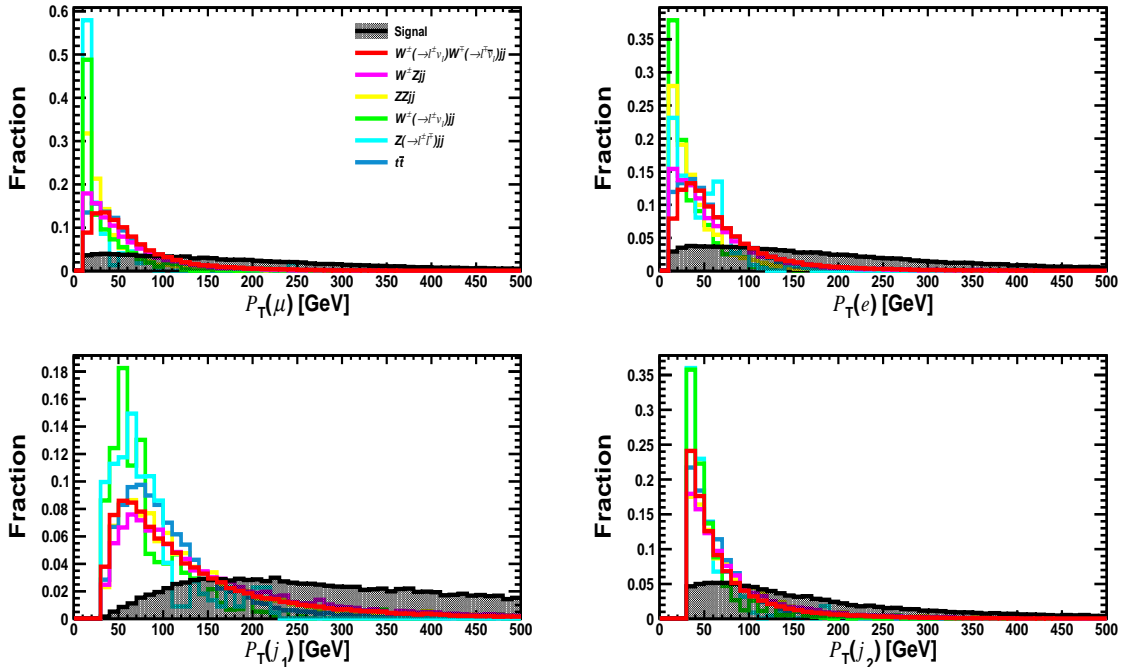
### B.3 Selection efficiencies

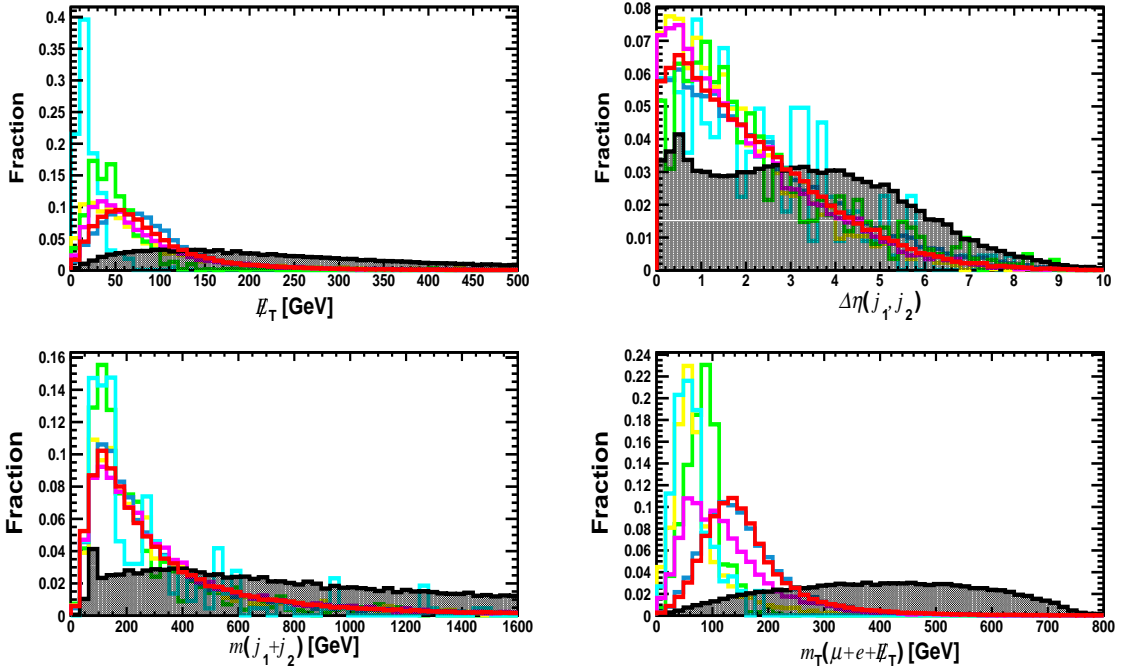
$m_a$	selection	signal	$W^\pm Zjj$	$ZZjj$	$Z(\rightarrow \mu^+\mu^-)jj$	$t\bar{t}$	$W^\pm(\rightarrow \mu^\pm \nu_\mu)W^\mp jj$	$W^\pm(\rightarrow \mu^\pm \nu_\mu)jj$	$W^\pm W^\pm jj$	$W^\pm W^\pm W^\mp$
170 GeV	preselection	$2.94 \times 10^{-3}$	$3.15 \times 10^{-4}$	$3.66 \times 10^{-5}$	$8.57 \times 10^{-6}$	$2.57 \times 10^{-5}$	$5.40 \times 10^{-5}$	$2.97 \times 10^{-5}$	$6.19 \times 10^{-3}$	$3.87 \times 10^{-3}$
	$BDT > 0.069$	$4.56 \times 10^{-1}$	$4.83 \times 10^{-2}$	$3.28 \times 10^{-2}$	—	$6.02 \times 10^{-3}$	$2.96 \times 10^{-2}$	$2.79 \times 10^{-3}$	$6.22 \times 10^{-2}$	$1.51 \times 10^{-1}$
200 GeV	preselection	$3.43 \times 10^{-3}$	$3.15 \times 10^{-4}$	$3.66 \times 10^{-5}$	$8.57 \times 10^{-6}$	$2.57 \times 10^{-5}$	$5.40 \times 10^{-5}$	$2.97 \times 10^{-5}$	$6.19 \times 10^{-3}$	$3.87 \times 10^{-3}$
	$BDT > 0.049$	$6.16 \times 10^{-1}$	$1.10 \times 10^{-1}$	$8.20 \times 10^{-2}$	—	$4.22 \times 10^{-2}$	$2.96 \times 10^{-2}$	$2.79 \times 10^{-3}$	$1.36 \times 10^{-1}$	$3.00 \times 10^{-1}$
300 GeV	preselection	$4.44 \times 10^{-3}$	$3.15 \times 10^{-4}$	$3.66 \times 10^{-5}$	$8.57 \times 10^{-6}$	$2.57 \times 10^{-5}$	$5.40 \times 10^{-5}$	$2.97 \times 10^{-5}$	$6.19 \times 10^{-3}$	$3.87 \times 10^{-3}$
	$BDT > 0.086$	$5.48 \times 10^{-1}$	$4.12 \times 10^{-2}$	$2.19 \times 10^{-2}$	—	—	$7.41 \times 10^{-3}$	$2.79 \times 10^{-3}$	$5.27 \times 10^{-2}$	$1.49 \times 10^{-1}$
400 GeV	preselection	$4.41 \times 10^{-3}$	$3.15 \times 10^{-4}$	$3.66 \times 10^{-5}$	$8.57 \times 10^{-6}$	$2.57 \times 10^{-5}$	$5.40 \times 10^{-5}$	$2.97 \times 10^{-5}$	$6.19 \times 10^{-3}$	$3.87 \times 10^{-3}$
	$BDT > 0.083$	$5.29 \times 10^{-1}$	$3.70 \times 10^{-2}$	$3.28 \times 10^{-2}$	—	$6.02 \times 10^{-3}$	—	$2.79 \times 10^{-3}$	$4.36 \times 10^{-2}$	$1.35 \times 10^{-1}$
600 GeV	preselection	$5.09 \times 10^{-3}$	$3.15 \times 10^{-4}$	$3.66 \times 10^{-5}$	$8.57 \times 10^{-6}$	$2.57 \times 10^{-5}$	$5.40 \times 10^{-5}$	$2.97 \times 10^{-5}$	$6.19 \times 10^{-3}$	$3.87 \times 10^{-3}$
	$BDT > 0.099$	$6.50 \times 10^{-1}$	$1.92 \times 10^{-2}$	$2.19 \times 10^{-2}$	—	—	$7.41 \times 10^{-3}$	—	$2.47 \times 10^{-2}$	$6.10 \times 10^{-2}$
900 GeV	preselection	$5.07 \times 10^{-3}$	$3.15 \times 10^{-4}$	$3.66 \times 10^{-5}$	$8.57 \times 10^{-6}$	$2.57 \times 10^{-5}$	$5.40 \times 10^{-5}$	$2.97 \times 10^{-5}$	$6.19 \times 10^{-3}$	$3.87 \times 10^{-3}$
	$BDT > 0.121$	$6.70 \times 10^{-1}$	$5.08 \times 10^{-3}$	—	—	—	—	—	$9.56 \times 10^{-3}$	$2.06 \times 10^{-2}$
1400 GeV	preselection	$5.13 \times 10^{-3}$	$3.15 \times 10^{-4}$	$3.66 \times 10^{-5}$	$8.57 \times 10^{-6}$	$2.57 \times 10^{-5}$	$5.40 \times 10^{-5}$	$2.97 \times 10^{-5}$	$6.19 \times 10^{-3}$	$3.87 \times 10^{-3}$
	$BDT > 0.120$	$8.05 \times 10^{-1}$	$2.54 \times 10^{-3}$	—	—	—	$7.41 \times 10^{-3}$	—	$6.78 \times 10^{-3}$	$1.38 \times 10^{-2}$
1800 GeV	preselection	$5.18 \times 10^{-3}$	$3.15 \times 10^{-4}$	$3.66 \times 10^{-5}$	$8.57 \times 10^{-6}$	$2.57 \times 10^{-5}$	$5.40 \times 10^{-5}$	$2.97 \times 10^{-5}$	$6.19 \times 10^{-3}$	$3.87 \times 10^{-3}$
	$BDT > 0.152$	$7.80 \times 10^{-1}$	$1.13 \times 10^{-3}$	—	—	—	—	—	$2.52 \times 10^{-3}$	$5.49 \times 10^{-3}$
2200 GeV	preselection	$5.17 \times 10^{-3}$	$3.15 \times 10^{-4}$	$3.66 \times 10^{-5}$	$8.57 \times 10^{-6}$	$2.57 \times 10^{-5}$	$5.40 \times 10^{-5}$	$2.97 \times 10^{-5}$	$6.19 \times 10^{-3}$	$3.87 \times 10^{-3}$
	$BDT > 0.120$	$8.98 \times 10^{-1}$	$1.98 \times 10^{-3}$	—	—	—	—	—	$4.52 \times 10^{-3}$	$7.62 \times 10^{-3}$
3000 GeV	preselection	$5.20 \times 10^{-3}$	$3.15 \times 10^{-4}$	$3.66 \times 10^{-5}$	$8.57 \times 10^{-6}$	$2.57 \times 10^{-5}$	$5.40 \times 10^{-5}$	$2.97 \times 10^{-5}$	$6.19 \times 10^{-3}$	$3.87 \times 10^{-3}$
	$BDT > 0.080$	$9.57 \times 10^{-1}$	$1.69 \times 10^{-3}$	—	—	—	$7.41 \times 10^{-3}$	—	$5.75 \times 10^{-3}$	$8.66 \times 10^{-3}$
5000 GeV	preselection	$5.42 \times 10^{-3}$	$3.15 \times 10^{-4}$	$3.66 \times 10^{-5}$	$8.57 \times 10^{-6}$	$2.57 \times 10^{-5}$	$5.40 \times 10^{-5}$	$2.97 \times 10^{-5}$	$6.19 \times 10^{-3}$	$3.87 \times 10^{-3}$
	$BDT > 0.080$	$9.80 \times 10^{-1}$	$1.13 \times 10^{-3}$	—	—	—	—	—	$2.45 \times 10^{-3}$	$3.49 \times 10^{-3}$
10000 GeV	preselection	$5.30 \times 10^{-3}$	$3.15 \times 10^{-4}$	$3.66 \times 10^{-5}$	$8.57 \times 10^{-6}$	$2.57 \times 10^{-5}$	$5.40 \times 10^{-5}$	$2.97 \times 10^{-5}$	$6.19 \times 10^{-3}$	$3.87 \times 10^{-3}$
	$BDT > 0.030$	$9.93 \times 10^{-1}$	$1.13 \times 10^{-3}$	—	—	—	—	—	$7.11 \times 10^{-4}$	$2.07 \times 10^{-3}$
20000 GeV	preselection	$5.43 \times 10^{-3}$	$3.15 \times 10^{-4}$	$3.66 \times 10^{-5}$	$8.57 \times 10^{-6}$	$2.57 \times 10^{-5}$	$5.40 \times 10^{-5}$	$2.97 \times 10^{-5}$	$6.19 \times 10^{-3}$	$3.87 \times 10^{-3}$
	$BDT > 0.050$	$9.97 \times 10^{-1}$	$8.47 \times 10^{-4}$	—	—	—	—	—	$1.29 \times 10^{-4}$	$5.17 \times 10^{-4}$

**Table 7:** Selection efficiencies of the preselection and BDT criteria for the signal and background processes at the SppC/FCC-hh with  $\sqrt{s} = 100$  TeV, assuming different ALP masses. Here, “—” indicates that the yield becomes negligible with  $\mathcal{L} = 20 \text{ ab}^{-1}$ .

## C Details of the $W^+W^-jj$ analyses

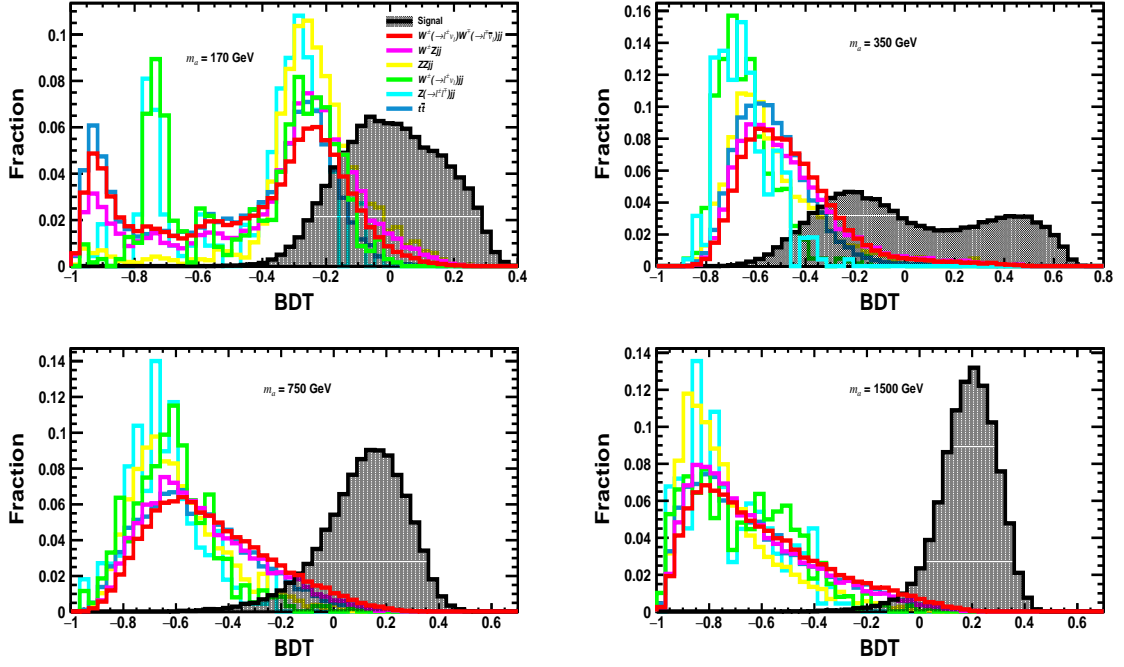
### C.1 Distributions of representative observables





**Figure 17:** Distributions of representative observables of the signal (black, dashed) and the six background processes at the SppC / FCC-hh with  $\sqrt{s} = 100$  TeV, assuming  $m_a = 750$  GeV.

## C.2 Distributions of BDT responses



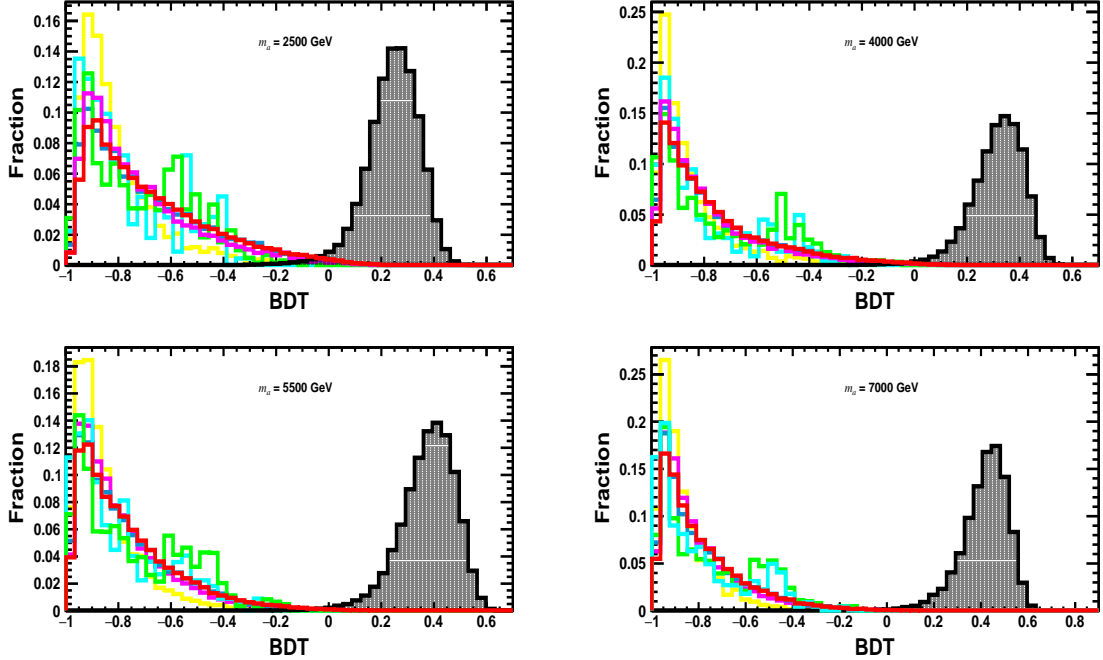


**Figure 18:** Distributions of BDT responses after applying the preselection criteria for the signal (black, shaded) and background processes at the SppC / FCC-hh with  $\sqrt{s} = 100$  TeV for representative  $m_a$  values.

### C.3 Selection efficiencies

$m_a$ [GeV]	BDT	signal	$W^+ (\rightarrow \ell^+ \nu) W^- (\rightarrow \ell^- \bar{\nu}) jj$	$WZjj$	$ZZjj$	$t\bar{t}$
170	0.047	$4.05 \times 10^{-1}$	$1.20 \times 10^{-2}$	$2.62 \times 10^{-2}$	$3.43 \times 10^{-2}$	$1.99 \times 10^{-3}$
185	0.126	$3.45 \times 10^{-1}$	$8.88 \times 10^{-3}$	$1.93 \times 10^{-2}$	$2.66 \times 10^{-2}$	$1.39 \times 10^{-3}$
200	0.038	$4.22 \times 10^{-1}$	$2.10 \times 10^{-2}$	$3.72 \times 10^{-2}$	$4.70 \times 10^{-2}$	$3.90 \times 10^{-3}$
225	-0.086	$5.07 \times 10^{-1}$	$4.01 \times 10^{-2}$	$5.77 \times 10^{-2}$	$6.36 \times 10^{-2}$	$8.48 \times 10^{-2}$
250	-0.132	$5.40 \times 10^{-1}$	$5.39 \times 10^{-2}$	$7.06 \times 10^{-2}$	$7.09 \times 10^{-2}$	$1.30 \times 10^{-3}$
350	0.256	$2.85 \times 10^{-1}$	$1.06 \times 10^{-2}$	$9.57 \times 10^{-3}$	$1.19 \times 10^{-2}$	$1.65 \times 10^{-3}$
750	0.096	$5.91 \times 10^{-1}$	$1.43 \times 10^{-2}$	$7.35 \times 10^{-3}$	$1.16 \times 10^{-3}$	$5.02 \times 10^{-3}$
1500	0.162	$6.14 \times 10^{-1}$	$2.03 \times 10^{-3}$	$1.16 \times 10^{-3}$	—	$5.19 \times 10^{-4}$
2500	0.165	$8.08 \times 10^{-1}$	$1.09 \times 10^{-3}$	$4.83 \times 10^{-4}$	—	$3.46 \times 10^{-4}$
4000	0.199	$8.86 \times 10^{-1}$	$5.00 \times 10^{-4}$	$3.87 \times 10^{-4}$	—	$8.66 \times 10^{-5}$
5500	0.200	$9.39 \times 10^{-1}$	$2.93 \times 10^{-4}$	$9.67 \times 10^{-5}$	—	$8.66 \times 10^{-5}$
7000	0.205	$9.62 \times 10^{-1}$	$2.59 \times 10^{-4}$	—	—	$8.66 \times 10^{-5}$

**Table 8:** Selection efficiencies of the BDT cut for both signal and background processes at the SppC/FCC-hh with  $\sqrt{s} = 100$  TeV, assuming different ALP masses. The second column gives the lower threshold of the BDT response, and “—” indicates that the number of events becomes negligible with  $\mathcal{L} = 20$  ab $^{-1}$ .

## Acknowledgments

We thank Bin Diao and Ye Lu for helpful discussions. Z.D., J.F. and K.W. are supported by the National Natural Science Foundation of China under grant no. 11905162, the Excellent Young Talents Program of the Wuhan University of Technology under grant no. 40122102, and the research program of the Wuhan University of Technology under grants no. 2020IB024 and 104972025KFYjc0101. Y.N.M. and Y.X. are supported by the National Natural Science Foundation of China under grant no. 12205227. The simulation and analysis work of this article was completed with the computational cluster provided by the Theoretical Physics Group at the Department of Physics, School of Physics and Mechanics, Wuhan University of Technology.

**Note added.** Following standard practice in high-energy physics, authors are listed in strict alphabetical order by surname. This ordering should not be interpreted as indicating any ranking of contribution, seniority, or leadership. All authors contributed equally to this work.

## References

- [1] R.D. Peccei and H.R. Quinn, *CP Conservation in the Presence of Instantons*, *Phys. Rev. Lett.* **38** (1977) 1440.
- [2] R.D. Peccei and H.R. Quinn, *Constraints Imposed by CP Conservation in the Presence of Instantons*, *Phys. Rev. D* **16** (1977) 1791.
- [3] S. Weinberg, *A New Light Boson?*, *Phys. Rev. Lett.* **40** (1978) 223.
- [4] F. Wilczek, *Problem of Strong P and T Invariance in the Presence of Instantons*, *Phys. Rev. Lett.* **40** (1978) 279.
- [5] J.E. Kim, *Weak Interaction Singlet and Strong CP Invariance*, *Phys. Rev. Lett.* **43** (1979) 103.
- [6] A.R. Zhitnitsky, *On Possible Suppression of the Axion Hadron Interactions. (In Russian)*, *Sov. J. Nucl. Phys.* **31** (1980) 260.
- [7] M. Dine, W. Fischler and M. Srednicki, *A Simple Solution to the Strong CP Problem with a Harmless Axion*, *Phys. Lett. B* **104** (1981) 199.
- [8] M. Dine, *TASI lectures on the strong CP problem*, in *Theoretical Advanced Study Institute in Elementary Particle Physics (TASI 2000): Flavor Physics for the Millennium*, pp. 349–369, 6, 2000 [[hep-ph/0011376](#)].
- [9] J.E. Kim and G. Carosi, *Axions and the Strong CP Problem*, *Rev. Mod. Phys.* **82** (2010) 557 [[0807.3125](#)].
- [10] J.E. Kim, *A Review on axions and the strong CP problem*, *AIP Conf. Proc.* **1200** (2010) 83 [[0909.3908](#)].
- [11] J. Quevillon and C. Smith, *Axions are blind to anomalies*, *Eur. Phys. J. C* **79** (2019) 822 [[1903.12559](#)].

[12] A. Hook, S. Kumar, Z. Liu and R. Sundrum, *High Quality QCD Axion and the LHC*, *Phys. Rev. Lett.* **124** (2020) 221801 [[1911.12364](#)].

[13] P. Svrcek and E. Witten, *Axions In String Theory*, *JHEP* **06** (2006) 051 [[hep-th/0605206](#)].

[14] I.G. Irastorza and J. Redondo, *New experimental approaches in the search for axion-like particles*, *Prog. Part. Nucl. Phys.* **102** (2018) 89 [[1801.08127](#)].

[15] L. Di Luzio, M. Giannotti, E. Nardi and L. Visinelli, *The landscape of QCD axion models*, *Phys. Rept.* **870** (2020) 1 [[2003.01100](#)].

[16] K. Choi, S.H. Im and C. Sub Shin, *Recent Progress in the Physics of Axions and Axion-Like Particles*, *Ann. Rev. Nucl. Part. Sci.* **71** (2021) 225 [[2012.05029](#)].

[17] K. Mimasu and V. Sanz, *ALPs at Colliders*, *JHEP* **06** (2015) 173 [[1409.4792](#)].

[18] J. Jaeckel and M. Spannowsky, *Probing MeV to 90 GeV axion-like particles with LEP and LHC*, *Phys. Lett. B* **753** (2016) 482 [[1509.00476](#)].

[19] J. Liu, L.-T. Wang, X.-P. Wang and W. Xue, *Exposing the dark sector with future Z factories*, *Phys. Rev. D* **97** (2018) 095044 [[1712.07237](#)].

[20] M. Bauer, M. Neubert and A. Thamm, *Collider Probes of Axion-Like Particles*, *JHEP* **12** (2017) 044 [[1708.00443](#)].

[21] M.J. Dolan, T. Ferber, C. Hearty, F. Kahlhoefer and K. Schmidt-Hoberg, *Revised constraints and Belle II sensitivity for visible and invisible axion-like particles*, *JHEP* **12** (2017) 094 [[1709.00009](#)].

[22] M. Bauer, M. Heiles, M. Neubert and A. Thamm, *Axion-Like Particles at Future Colliders*, *Eur. Phys. J. C* **79** (2019) 74 [[1808.10323](#)].

[23] M.B. Gavela, J.M. No, V. Sanz and J.F. de Trocóniz, *Nonresonant Searches for Axionlike Particles at the LHC*, *Phys. Rev. Lett.* **124** (2020) 051802 [[1905.12953](#)].

[24] D. d'Enterria, *Collider constraints on axion-like particles*, in *Workshop on Feebly Interacting Particles*, 2, 2021 [[2102.08971](#)].

[25] P. Agrawal et al., *Feebly-interacting particles: FIPs 2020 workshop report*, *Eur. Phys. J. C* **81** (2021) 1015 [[2102.12143](#)].

[26] H.-Y. Zhang, C.-X. Yue, Y.-C. Guo and S. Yang, *Searching for axionlike particles at future electron-positron colliders*, *Phys. Rev. D* **104** (2021) 096008 [[2103.05218](#)].

[27] M. Tian, Z.S. Wang and K. Wang, *Search for long-lived axions with far detectors at future lepton colliders*, [2201.08960](#).

[28] F.A. Ghebretinsa, Z.S. Wang and K. Wang, *Probing axion-like particles coupling to gluons at the LHC*, *JHEP* **07** (2022) 070 [[2203.01734](#)].

[29] A. de Giorgi, L. Merlo and J.-L. Tastet, *Probing HNL-ALP couplings at colliders*, *Fortsch. Phys.* **71** (2023) 2300027 [[2212.11290](#)].

[30] H. Wang, C.-X. Yue, Y.-C. Guo, X.-J. Cheng and X.-Y. Li, *Prospects for searching for axion-like particles at the CEPC*, *J. Phys. G* **49** (2022) 115002.

[31] R. Schäfer, F. Tillinger and S. Westhoff, *Near or far detectors? A case study for long-lived particle searches at electron-positron colliders*, *Phys. Rev. D* **107** (2023) 076022 [[2202.11714](#)].

[32] G. Galanti and M. Roncadelli, *Axion-like Particles Implications for High-Energy Astrophysics*, *Universe* **8** (2022) 253 [[2205.00940](#)].

[33] K. Cheung and C.J. Ouseph, *Axionlike particle search at Higgs factories*, *Phys. Rev. D* **108** (2023) 035003 [[2303.16514](#)].

[34] C. Antel et al., *Feebly-interacting particles: FIPs 2022 Workshop Report*, *Eur. Phys. J. C* **83** (2023) 1122 [[2305.01715](#)].

[35] P.S.B. Dev, J.-F. Fortin, S.P. Harris, K. Sinha and Y. Zhang, *First Constraints on the Photon Coupling of Axionlike Particles from Multimessenger Studies of the Neutron Star Merger GW170817*, *Phys. Rev. Lett.* **132** (2024) 101003 [[2305.01002](#)].

[36] T. Biswas, *Probing the interactions of axion-like particles with electroweak bosons and the higgs boson in the high energy regime at lhc*, *JHEP* **05** (2024) 081 [[2312.05992](#)].

[37] C.-X. Yue, H. Wang, X.-J. Cheng and Y.-Q. Wang, *Sensitivity of the future e-p collider to the coupling of axionlike particles with vector bosons*, *Phys. Rev. D* **107** (2023) 115025 [[2305.19561](#)].

[38] C.-X. Yue, H. Wang and Y.-Q. Wang, *Detecting the coupling of axion-like particles with fermions at the ILC*, *Phys. Lett. B* **848** (2024) 138368 [[2311.16768](#)].

[39] R. Balkin, O. Hen, W. Li, H. Liu, T. Ma, Y. Soreq et al., *Probing axion-like particles at the Electron-Ion Collider*, *JHEP* **02** (2024) 123 [[2310.08827](#)].

[40] F. Esser, M. Madigan, V. Sanz and M. Ubiali, *On the coupling of axion-like particles to the top quark*, *JHEP* **09** (2023) 063 [[2303.17634](#)].

[41] Y. Lu, Y.-n. Mao, K. Wang and Z.S. Wang, *LAYCAST: LAYered CAvern Surface Tracker at future electron-positron colliders*, [2406.05770](#).

[42] Q. Qiu, Y. Gao, H.-j. Tian, K. Wang, Z. Wang and X.-M. Yang, *Wide binary evaporation by dark solitons: implications from the GAIA catalog*, *JCAP* **02** (2025) 001 [[2404.18099](#)].

[43] K. Cheung, F.-T. Chung, G. Cottin and Z.S. Wang, *Quark flavor violation and axion-like particles from top-quark decays at the LHC*, *JHEP* **07** (2024) 209 [[2404.06126](#)].

[44] F. Esser, M. Madigan, A. Salas-Bernardez, V. Sanz and M. Ubiali, *Di-Higgs production via axion-like particles*, *JHEP* **10** (2024) 164 [[2404.08062](#)].

[45] Z. Wang and Y. Gao, *Axion minicluster halo limits from wide binary disruption*, *Phys. Rev. D* **111** (2025) 043042 [[2409.02468](#)].

[46] M.B. Marcos, A. de Giorgi, L. Merlo and J.-L. Tastet, *ALPs and HNLs at LHC and Muon Colliders: Uncovering New Couplings and Signals*, *SciPost Phys.* **18** (2025) 084 [[2407.14970](#)].

[47] G. Yang, T. Wang and G.-L. Wang, *Probing axion-like particles in leptonic decays of heavy mesons\**, *Chin. Phys. C* **49** (2025) 013109 [[2407.05298](#)].

[48] H. Li, Q. Wu and G. Zhang, *Single axion-like particles production in the  $\gamma\gamma$  channel at high energy muon colliders*, *Mod. Phys. Lett. A* **39** (2024) 2450113.

[49] S.C. İnan and A.V. Kisseelev, *Analysis of axion-like particles in a top-quark pair production at the CLIC*, [2501.15500](#).

[50] C.-X. Yue, X.-Y. Li, M.-S.-Y. Wang and Y.-Y. Bu, *Probing the couplings of an axionlike particle with leptons via three-lepton final state processes at future e-p colliders*, *Phys. Rev. D* **111** (2025) 075015 [[2503.03179](#)].

[51] X. Ai et al., *New physics search at the CEPC: a general perspective*, *Chin. Phys. C* **49** (2025) 123108 [[2505.24810](#)].

[52] S.-Y. Wang, Y.-P. Jiao, H.-H. Zhang and G. Cacciapaglia, *Probing Long-Lived Photophobic Axion-Like Particles via Prompt Leptons and Mono-gamma at FCC-ee and CEPC*, [2509.17718](#).

[53] S.-s. Bao, Y. Ma, Y. Wu, K. Xie and H. Zhang, *Light axion-like particles at future lepton colliders*, *JHEP* **10** (2025) 122 [[2505.10023](#)].

[54] J. Alda, M. Fuentes Zamoro, L. Merlo, X. Ponce Díaz and S. Rigolin, *Comprehensive ALP Searches in Meson Decays*, [2507.19578](#).

[55] Z. Wang and Y. Gao, *Axion Star Bosenova in Axion Miniclusters*, [2508.14535](#).

[56] R. Bedi, T. Gherghetta, S. Kumar, P. Li and Z. Liu, *Heavy QCD Axions at High-Energy Muon Colliders*, [2509.10605](#).

[57] M. Figliolia, F. Grippa, G. Lambiase and L. Visinelli, *Gravitational Signatures of Axion Dark Matter via Parity-Violating Interactions*, [2509.12038](#).

[58] C.-X. Yue, X.-Y. Li, S. Yang and M.-S.-Y. Wang, *Searching for long-lived axion-like particles via displaced vertices at the HL-LHC*, [2510.24097](#).

[59] F. Esser, A. Salas-Bernardez, M. Ubiali and V. Sanz, *A global analysis of ALP-mediated multiboson production at the LHC*, [2510.24873](#).

[60] J. Butterworth, M. Cullingworth, J. Egan, F. Esser, V. Sanz and M. Ubiali, *Probing the coupling of axions to tops and gluons with LHC measurements*, [2508.21660](#).

[61] CMS collaboration, *Evidence for light-by-light scattering and searches for axion-like particles in ultraperipheral PbPb collisions at  $\sqrt{s_{\text{NN}}} = 5.02$  TeV*, *Phys. Lett. B* **797** (2019) 134826 [[1810.04602](#)].

[62] BELLE-II collaboration, *Search for Axion-Like Particles produced in  $e^+e^-$  collisions at Belle II*, *Phys. Rev. Lett.* **125** (2020) 161806 [[2007.13071](#)].

[63] ATLAS collaboration, *Measurement of light-by-light scattering and search for axion-like particles with  $2.2 \text{ nb}^{-1}$  of Pb+Pb data with the ATLAS detector*, *JHEP* **03** (2021) 243 [[2008.05355](#)].

[64] ATLAS collaboration, *Search for boosted diphoton resonances in the 10 to 70 GeV mass range using  $138 \text{ fb}^{-1}$  of 13 TeV pp collisions with the ATLAS detector*, *JHEP* **07** (2023) 155 [[2211.04172](#)].

[65] BESIII collaboration, *Search for an axion-like particle in radiative  $J/\psi$  decays*, *Phys. Lett. B* **838** (2023) 137698 [[2211.12699](#)].

[66] BESIII collaboration, *Search for diphoton decays of an axionlike particle in radiative  $J/\psi$  decays*, *Phys. Rev. D* **110** (2024) L031101 [[2404.04640](#)].

[67] CMS collaboration, *Measurement of light-by-light scattering and the Breit-Wheeler process*,

and search for axion-like particles in ultraperipheral  $PbPb$  collisions at  $\sqrt{s_{NN}} = 5.02$  TeV, *JHEP* **08** (2025) 006 [[2412.15413](#)].

- [68] PARTICLE DATA GROUP collaboration, *Review of particle physics*, *Phys. Rev. D* **110** (2024) 030001.
- [69] C. O'HARE, *cajohare/AxionLimits: AxionLimits*, <https://doi.org/10.5281/zenodo.3932429> (2024) .
- [70] N. Craig, A. Hook and S. Kasko, *The Photophobic ALP*, *JHEP* **09** (2018) 028 [[1805.06538](#)].
- [71] N. Fonseca, E. Morgante and G. Servant, *Higgs relaxation after inflation*, *JHEP* **10** (2018) 020 [[1805.04543](#)].
- [72] A. Hook and G. Marques-Tavares, *Relaxation from particle production*, *JHEP* **12** (2016) 101 [[1607.01786](#)].
- [73] CDF collaboration, *High-precision measurement of the  $W$  boson mass with the CDF II detector*, *Science* **376** (2022) 170.
- [74] M. Aiko and M. Endo, *Electroweak precision test of axion-like particles*, *JHEP* **05** (2023) 147 [[2302.11377](#)].
- [75] J. Bonilla, I. Brivio, J. Machado-Rodríguez and J.F. de Trocóniz, *Nonresonant searches for axion-like particles in vector boson scattering processes at the LHC*, *JHEP* **06** (2022) 113 [[2202.03450](#)].
- [76] M. Aiko, M. Endo and K. Fridell, *Heavy photophobic ALP at the LHC*, *JHEP* **06** (2024) 194 [[2401.13323](#)].
- [77] Z. Ding, Y.-n. Mao and K. Wang, *Search for the  $\gamma Z$  decay mode of heavy photophobic axion-like particles at the LHC*, *JHEP* **06** (2025) 087 [[2411.08660](#)].
- [78] Y.-n. Mao, K. Wang and Y. Xiong, *Sensitivities of new resonance couplings to  $W$ -bosons at the LHC\**, *Chin. Phys. B* **49** (2025) 083106 [[2411.14041](#)].
- [79] J. Feng, Y.-n. Mao and K. Wang, *Discovery prospects for photophobic axion-like particles in the  $WWjj$  final state at the High-Luminosity LHC*, [2511.21003](#).
- [80] CEPC-SPPC Preliminary Conceptual Design Report. 2. Accelerator, .
- [81] M. Benedikt and F. Zimmermann, *Proton Colliders at the Energy Frontier*, *Nucl. Instrum. Meth. A* **907** (2018) 200 [[1803.09723](#)].
- [82] CEPC STUDY GROUP collaboration, *CEPC Conceptual Design Report: Volume 1 - Accelerator*, [1809.00285](#).
- [83] CEPC STUDY GROUP collaboration, *CEPC Technical Design Report: Accelerator*, *Radiat. Detect. Technol. Methodol.* **8** (2024) 1 [[2312.14363](#)].
- [84] FCC collaboration, *FCC-hh: The Hadron Collider: Future Circular Collider Conceptual Design Report Volume 3*, *Eur. Phys. J. ST* **228** (2019) 755.
- [85] FCC collaboration, *The hadron collider FCC-hh: Extended conceptual design report*, .
- [86] H. Georgi, D.B. Kaplan and L. Randall, *Manifesting the Invisible Axion at Low-energies*, *Phys. Lett. B* **169** (1986) 73.

[87] M. Bauer, M. Neubert, S. Renner, M. Schnubel and A. Thamm, *The Low-Energy Effective Theory of Axions and ALPs*, *JHEP* **04** (2021) 063 [[2012.12272](#)].

[88] J. Bonilla, I. Brivio, M.B. Gavela and V. Sanz, *One-loop corrections to ALP couplings*, *JHEP* **11** (2021) 168 [[2107.11392](#)].

[89] I. Brivio, M.B. Gavela, L. Merlo, K. Mimasu, J.M. No, R. del Rey et al., *ALPs Effective Field Theory and Collider Signatures*, *Eur. Phys. J. C* **77** (2017) 572 [[1701.05379](#)].

[90] C. Degrande, C. Duhr, B. Fuks, D. Grellscheid, O. Mattelaer and T. Reiter, *UFO - The Universal FeynRules Output*, *Comput. Phys. Commun.* **183** (2012) 1201 [[1108.2040](#)].

[91] J. Alwall, R. Frederix, S. Frixione, V. Hirschi, F. Maltoni, O. Mattelaer et al., *The automated computation of tree-level and next-to-leading order differential cross sections, and their matching to parton shower simulations*, *JHEP* **07** (2014) 079 [[1405.0301](#)].

[92] R.D. Ball et al., *Parton distributions with LHC data*, *Nucl. Phys. B* **867** (2013) 244 [[1207.1303](#)].

[93] C. Bierlich et al., *A comprehensive guide to the physics and usage of PYTHIA 8.3*, *SciPost Phys. Codeb.* **2022** (2022) 8 [[2203.11601](#)].

[94] DELPHES 3 collaboration, *DELPHES 3, A modular framework for fast simulation of a generic collider experiment*, *JHEP* **02** (2014) 057 [[1307.6346](#)].

[95] M. Cacciari, G.P. Salam and G. Soyez, *FastJet User Manual*, *Eur. Phys. J. C* **72** (2012) 1896 [[1111.6097](#)].

[96] M. Cacciari, G.P. Salam and G. Soyez, *The anti- $k_t$  jet clustering algorithm*, *JHEP* **04** (2008) 063 [[0802.1189](#)].

[97] TMVA collaboration, *TMVA - Toolkit for Multivariate Data Analysis*, [physics/0703039](#).

[98] G. Cowan, K. Cranmer, E. Gross and O. Vitells, *Asymptotic formulae for likelihood-based tests of new physics*, *Eur. Phys. J. C* **71** (2011) 1554 [[1007.1727](#)].

[99] ATLAS collaboration, *Formulae for Estimating Significance*, Tech. Rep. CERN, Geneva (2020), [DOI](#).

[100] P.N. Bhattacharjee, S.P. Martin and J.D. Wells, *Criteria for projected discovery and exclusion sensitivities of counting experiments*, *Eur. Phys. J. C* **81** (2021) 123 [[2009.07249](#)].

[101] J. Thaler, “How to read lhc olympics data files (lhco format).” <https://madgraph.phys.ucl.ac.be/Manual/lhco.html>, 2006.

[102] T. Han, *Collider phenomenology: Basic knowledge and techniques*, in *Theoretical Advanced Study Institute in Elementary Particle Physics: Physics in  $D \geq 4$* , pp. 407–454, 8, 2005, [DOI](#) [[hep-ph/0508097](#)].

[103] CMS collaboration, *Measurement of inclusive and differential cross sections for  $W^+W^-$  production in proton–proton collisions at  $\sqrt{s} = 13.6$  TeV*, *Phys. Lett. B* **861** (2025) 139231 [[2406.05101](#)].